POLITECNICO DI TORINO
Repository ISTITUZIONALE

Ducted Fuel Injection: A Numerical Soot-Targeted Duct Geometry Optimization

Original
Ducted Fuel Injection: A Numerical Soot-Targeted Duct Geometry Optimization / Millo, F.; Piano, A.; Peiretti Paradisi, B.; Segatori, C.; Postrioti, L.; Pieracci, L.; Bianco, A.; Pesce, F. C.; Vassallo, A.. - In: SAE INTERNATIONAL JOURNAL OF ENGINES. - ISSN 1946-3936. - ELETTRONICO. - 15:2(2022). [10.4271/03-15-02-0014]

Availability:
This version is available at: 11583/2939207 since: 2021-11-22T09:46:29Z

Publisher:
SAE International

Published
DOI:10.4271/03-15-02-0014

Terms of use:

This article is made available under terms and conditions as specified in the corresponding bibliographic description in the repository

Publisher copyright

(Article begins on next page)

30 April 2026

Downloaded from SAE International by Torino Politecnico, Tuesday, September 28, 2021

ARTICLE INFO
Article ID: 03-15-02-0014
© 2022 Politecnico di Torino
doi:10.4271/03-15-02-0014

Ducted Fuel Injection: A Numerical Soot-Targeted Duct Geometry Optimization

Federico Millo,[1] Andrea Piano,[1] Benedetta Peiretti Paradisi,[1] Cristiano Segatori,[1] Lucio Postrioti,[2] Luca Pieracci,[2] Andrea Bianco,[3] Francesco Concetto Pesce,[4] and Alberto Vassallo[4]

[1]Politecnico di Torino, Italy
[2]Università degli Studi di Perugia, Italy
[3]POWERTECH Engineering, Italy
[4]PUNCH Torino (former General Motors Global Propulsion Systems), Italy

Abstract

Ducted Fuel Injection (DFI) is a recently developed concept to curtail soot formation in diesel flames and based on fuel injection along the axis of a small cylindrical pipe within the combustion chamber, enhancing mixture preparation upstream the autoignition zone. Experimental observations have shown a remarkable DFI effectiveness in soot mitigation; however, the mechanisms enabled by duct adoption are not yet fully clear, especially when different duct geometries are considered.

This article proposes an experiment-simulation coupled approach for the analysis of DFI in a constant volume vessel, operating in both non-reacting and reacting conditions. In particular, a previously calibrated three-dimensional computational fluid dynamics (*3D-CFD*) spray model was further validated against experimental liquid penetration considering different duct geometries, proving its reliability for testing duct geometrical variations. Afterward, the validated spray model was employed to investigate the influence of the main geometrical features (stand-off distance, duct length and diameter, inlet and outlet shape) on the ducted spray characteristics and on the combustion and emissions formation processes.

The reduction of both stand-off distance and duct length, up to the flow area limit in which the air entrainment is almost zeroed, leads to the best soot mitigation performance. Furthermore, a chamfer at the duct inlet enhances the duct adoption benefits due to improved air entrainment, confirming previous experimental observations. Thereby, it was possible to figure out an optimal duct configuration in terms of soot emission minimization by evaluating air entrainment and turbulent mixing at duct inlet and outlet, and flame lift-off length, achieving a soot mass curtailing of more than an order of magnitude.

History

Received: 15 May 2021
Revised: 21 Jul 2021
Accepted: 11 Aug 2021
e-Available: 14 Sep 2021

Keywords

Ducted fuel injection, Duct optimization, Diesel combustion, Soot mitigation, Computational fluid dynamics, Mixing, Spray

Citation

Millo, F., Piano, A., Peiretti Paradisi, B., Segatori, C. et al., "Ducted Fuel Injection: A Numerical Soot-Targeted Duct Geometry Optimization," *SAE Int. J. Engines* 15(2):2022, doi:10.4271/03-15-02-0014.

ISSN: 1946-3936
e-ISSN: 1946-3944

© 2022 Politecnico di Torino; Published by SAE International. This Open Access article is published under the terms of the Creative Commons Attribution License (http://creativecommons.org/licenses/by/4.0/), which permits distribution, and reproduction in any medium, provided that the original author(s) and the source are credited.

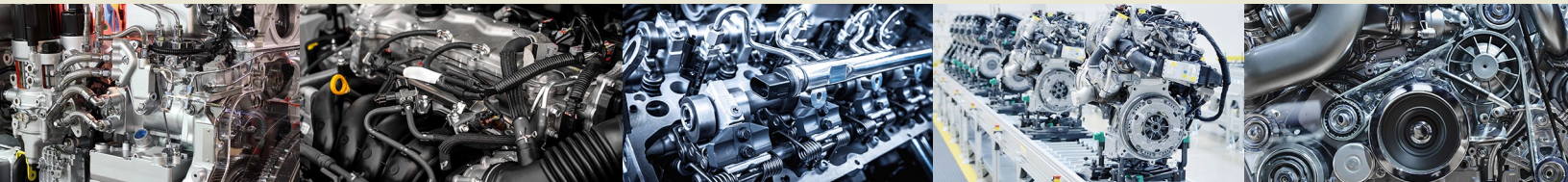

Downloaded from SAE International by Torino Politecnico, Tuesday, September 28, 2021

1. Introduction

Soot (or black carbon) emissions are toxic for human health [1] and are recognized as climate-forcing species, second only to carbon dioxide [2]. Compression-Ignition (CI) diesel engines are among the most contributors to the atmospheric pollution by soot in the transportation sector [3]; thus they are subjected to more and more stringent emissions regulations in the last years. Nonetheless, diesel engine characteristics, such as robustness, reliability, and high efficiency, are desirable for many applications in which the transfer of people and goods is required, both on-road and off-road. Therefore, to reduce the environmental impact, after-treatment systems are continuously under development for the reduction of Nitrogen Oxides (NOx) and Particulate Matter (PM) tailpipe emissions [4, 5]. However, the complexity and the cost of these systems are moving the research focus on the in-cylinder combustion process to prevent the formation of pollutants and reduce the requirements in terms of exhaust gas treatment.

When conventional Mixing-Controlled (MC) diesel combustion is considered, calibration efforts (e.g., Exhaust Gas Recirculation (EGR), swirl flap actuation, rail pressure) cannot simultaneously reduce NOx and soot emissions while keeping a high-efficiency level due to the well-known soot/NOx and efficiency/NOx trade-offs [6]. Thereby, advanced diesel combustion strategies, as Low-Temperature Combustion (LTC) [7], Homogeneous-Charge Compression-Ignition (HCCI) [8], and Reactivity-Controlled Compression-Ignition (RCCI) [9], are nowadays under investigations. These combustion concepts aim to enhance the premixing of the charge lowering both the equivalence ratio and the combustion temperature for avoiding the soot and NOx formation area in the Kamimoto-Bae diagram [10]. However, hard controllability, the increase in combustion noise, and the complex adaptation in the entire engine operating map make their applicability in series production challenging. Hence, in the context of the MC combustion approach, a different strategy to curtail soot particles formation emerged in the last decades, known as Leaner Lifted-Flame Combustion (LLFC), which aims to reach equivalence ratios below approximately two in the auto-ignition zone increasing the Lift-Off Length (LOL). It has been demonstrated that soot formation can effectively be prevented even at a high level of charge dilution, giving the opportunity of decreasing NOx formation without any detrimental effect on the combustion process [11]. This approach can be adopted at low loads, but unfortunately, when load increases and injectors with more than two orifices are employed, re-entrainment of hot combustion products and spray-to-spray interaction nullify the LLFC regime [12], highlighting the need for additional mixing-enhancement technology.

Therefore, during the last few years, the Ducted Fuel Injection (DFI) concept, patented by Sandia National Laboratories, was proposed: DFI is based on injecting fuel down the axis of a small cylindrical pipe in the combustion chamber in order to enable and sustain the LLFC. The initial proof-of-concept by Mueller et al. [13] has experimentally shown the remarkable DFI effectiveness in curtailing soot natural luminosity of two orders of magnitude with respect to the conventional free spray, in a constant-volume combustion-vessel considering Engine Combustion Network (ECN) Spray A operating conditions and using a reference duct with a 3 mm diameter, a 14 mm length, and a 2 mm gap from the injector tip. The subsequent work by Gehmlich et al. [14] confirmed such capability of DFI, measuring soot mass in the vessel throughout the combustion event and extending the temperature range, keeping constant the density. After that, DFI has been implemented in an engine combustion chamber (reference duct: 2 mm diameter, 12 mm length, 3 mm gap): three different studies conducted in an optical research CI engine by Nilsen et al. have shown that DFI attenuates engine-out soot emissions at low load by approximately an order of magnitude with respect to conventional diesel combustion [15] and breaks the soot/NOx trade-off with dilution at medium load (6.8 bar gross indicated mean effective pressure (IMEP)). In particular, DFI operation could meet the current on-road and off-road United States emissions standards on soot and NOx, without any specific after-treatment system using intake charge at 12% oxygen [16]. However, when tested at higher loads (about 10 bar IMEP), the DFI benefits tended to decrease [17], manifesting the requirement of a different calibration and, most of all, of an accurate duct design.

In order to correctly match the duct ability and the clean combustion needs, a comprehensive understanding of this innovative technology is necessary, focusing on the mechanisms involved in the soot formation mitigation process, which is not yet fully clear. Starting from the impact of DFI on the injection process, Li et al. [18, 19, 20] investigated the DFI macroscopic characteristics (reference duct: 2 mm diameter, 14 mm length, 2 mm gap) in non-reacting conditions via Schlieren imaging, finding that DFI penetrates more than the free spray, with a larger cone angle downstream of the duct and more fluctuating peripheries. Gehmlich et al. [14] analyzed a duct shape with a rounded inlet and a tapered outlet. This configuration was then employed by Svensson et al. [21], which parametrically analyzed DFI in a high-temperature pressure vessel varying stand-off distance and duct length and finding that the longest (14 mm length) and nearest to the injector tip (0.1 mm gap) duct was the most efficient geometry in reducing soot. However, the soot outcome was comparable with a totally different configuration (8 mm length, 4.5 mm gap) with a similar duct exit location.

In the complex framework of preliminary duct investigation and optimization, Computational Fluid Dynamics (CFD) can be a valid tool for deeply understanding the soot inhibition mechanisms enabled by DFI. Fitzgerald et al. [22] employed a computational combustion model (based on the Hiroyasu model for soot prediction) for DFI investigation,

Downloaded from SAE International by Torino Politecnico, Tuesday, September 28, 2021

after a qualitative correlation with the experimental trends observed in a high-temperature high-pressure vessel. They justified the DFI effectiveness suggesting that the ducted jet is richer and cooler inside the duct, leading to elevated turbulence levels at the duct outlet, which promotes mixing and a lower equivalence ratio at the LOL. Tanno et al. [23], after experimental tests of DFI in a rapid compression machine and numerical modeling, concluded that DFI homogenizes the mixture narrowing the equivalence ratio distribution because of the more air entrainment sent toward the spray core. Nilsen et al. [24] used a calibrated spray model in ECN Spray A operating conditions (non-reacting) to investigate DFI fluid mechanics and found that the presence of the duct enhances upstream air entrainment, but reduces the overall one. However, the promoted high mixing compensates, leading to a lower equivalence ratio both at the duct exit and at the LOL. Furthermore, they employed three different duct geometries, concluding that shorter ducts cause lower air entrainment inhibition and, thus, better equivalence ratio distribution at LOL. Millo et al. [25], after an extensive experimental campaign in a Constant Volume Vessel (CVV), calibrated and validated a spray model to deepen the knowledge on air entrainment and mixing enhancement by DFI. They confirmed the previous outcomes by quantifying the duct upstream air entrainment and showed that DFI, in non-reacting conditions, strongly raises the Turbulent Kinetic Energy (TKE), lowering and homogenizing the equivalence ratio distribution. Furthermore, a fully predictive combustion analysis, featuring the detailed soot Particulate Mimic model, confirmed that DFI drastically lowers soot formation without any detrimental effect on the other pollutant emissions. The same validated CFD setup was then exploited to assess DFI behavior compared to free spray for different engine calibration parameters in reacting CVV conditions [26]. It was found that DFI reduces its potential, increasing the surrounding mixture density, features a promising resistance to dilution and tremendously improves its soot formation mitigation mechanisms when rail pressure increases.

The present work employs the previously developed spray model [25], the detailed chemistry solver, and the Particulate Mimic model to conduct the first numerical work targeted to the optimization of the duct geometry, operating in a CVV in engine-like conditions. The spray model is further validated against experimental data to prove the capability of capturing the spray penetration when duct geometrical parameters are varied. Then the effects of stand-off distance, duct length, duct diameter, and duct inlet and outlet shapes are examined in both non-reacting and reacting conditions to analyze the air entrainment and turbulent mixing processes and their impact on the combustion and emission formation processes. Eventually, the optimal duct geometry is compared with the free spray configuration, highlighting a 94% soot reduction.

2. Experimental and Simulation Methodology

2.1. Experimental Setup

In order to support the parametric numerical analysis of the ducted spray in non-reacting and reacting conditions, a dedicated experimental campaign was carried out to appropriately validate the CONVERGE CFD numerical model. To this end, the numerical code validation described in [25] was extended focusing on the possible effects exerted by different injector-duct configurations on the spray evolving in a CVV at high temperature and high pressure. To simplify the parametric analysis of different duct configurations, a research one-hole (180 μm diameter) nozzle was installed on a standard Bosch CRI1 common rail injector, fed by commercial diesel fuel statically pressurized by a hydraulic press.

The numerical model was initialized in terms of fuel injection rate basing on the experimental campaign evidence as described in [25]. The injection rate was measured by a proprietary Injection Analyzer based on the Zeuch Method, which allows obtaining the single-shot-resolved measurement of injection rate profile and injected volume in any assigned operating condition. The measurement repetition for a statistically significant set of consecutive injector actuations (300 in the present campaign) allows the evaluation of the mean injection rate and injected volume, along with the injector operation dispersion. Further details about the used Injection Analyzer are reported in [27]. The spray drops sizing resulting from the spray evolution in high-temperature and high-pressure conditions was investigated by a Phase-Doppler Anemometry (PDA) system, composed of a Dantec FlowLite 1D laser source coupled with a Dantec BSA P80 processor. A schematic of the experimental apparatus for PDA measurements is reported in Figure 1 (left).

The used PDA allowed the detection of drops sizing and vertical velocity component 50 mm downstream the nozzle, both in non-evaporative (373 K) and evaporative (773 K) conditions in the pressurized test chamber (10 bar) for the free-evolving and the ducted spray configurations. The obtained sizing results were used for accurate calibration of the atomization and drop evolution sub-models adopted in CONVERGE CFD; further, the experimental evidence of the sizing analysis confirmed the significant effect exerted by the duct insertion on the spray drops evaporation, evidenced by the drastic reduction of the drops population (down to 50%) downstream the duct exit section, particularly with moderate injection pressure levels [25].

The spray global evolution with different duct configurations was investigated using the same CVV used for PDA analysis. A high-speed Complementary Metal Oxyde Semiconductor (CMOS) camera (Vision Research Miro 310 C) was used to acquire videos of the back-illuminated spray

Downloaded from SAE International by Torino Politecnico, Tuesday, September 28, 2021

FIGURE 1 Schematic of the experimental apparatus for PDA measurements (left) and Schlieren imaging (right).

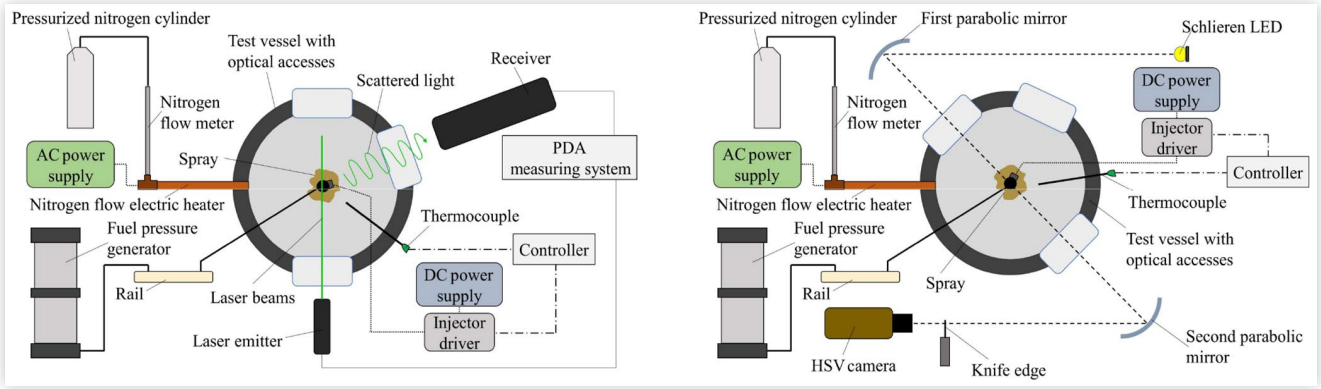

© Politecnico di Torino

evolving in the test vessel using two opposite rectangular quartz windows. A high-power LED (Luminus CBT-140) was used as a steady light source; two 6-inches parabolic mirrors positioned according to a classic Schlieren Z-configuration were used to obtain a parallel light beam crossing the CVV that was finally focused and acquired by the CMOS camera. The CMOS camera was operated at 50 kframe/s, with a 1 µs exposure time and a 128 × 320 resolution, offering a 50-mm-long field of view in the spray evolution plane. A schematic of the Schlieren imaging experimental system for spray global evolution measurements is depicted in Figure 1 (right). The 20 spray videos acquired in each tested operating condition were offline digitally analyzed by proprietary software developed in the LabVIEW™ Vision environment. By this procedure, single frames were extracted from the high-speed videos and binarized in order to locate the boundary of the spray liquid phase. The resulting 2-bit images were then further processed to compute the spray tip penetration and cone angle, according to the SAEJ2715 rule. This procedure was repeated at different elapsed timings from the injector actuation start, so to build spray mean penetration and cone angle curves as a function of time along with the corresponding shot-to-shot dispersion.

Moving to the different duct geometries, a proper nomenclature of the main duct geometrical parameters was introduced following the available literature concerning DFI. In Figure 2 stand-off distance (*G*), duct length (*L*), and duct diameter (*D*) are defined.

FIGURE 2 Main duct geometrical parameters: stand-off distance (*G*), duct length (*L*), and duct diameter (*D*).

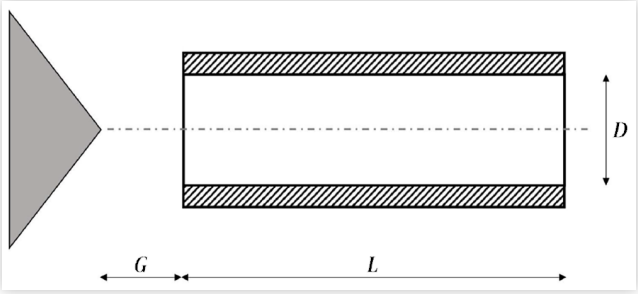

© Politecnico di Torino

In order to facilitate the analysis of different duct configurations, as described in [25], a modular design for the duct holder was adopted. Following this approach, different ducts can be easily installed with the duct inlet section positioned at a stand-off distance from the nozzle exit ranging from 0 to 4 mm; the global shape of the duct holder was defined to minimize its intrusiveness on the spray evolution and on the spray/duct interaction. In Table 1 the different configurations experimentally analyzed in terms of spray evolution are described; the *standard* configuration is coincident with the design analyzed in [25]. As can be seen, the effect of both duct length and duct inlet section distance from the nozzle hole were considered in the analysis; further, the distance from the nozzle hole to the duct outlet section was the same for *standard* and *shifted duct* configurations while it was significantly reduced for *short duct* configuration.

All the configurations reported in Table 1 were analyzed in terms of spray evolution with different rail pressure levels (400, 800, and 1200 bar); conditions in the CVV were set at 20 bar and 773 K. For the sake of brevity, only the results obtained at 1200 bar rail pressure are reported in Figure 3 in terms of penetration and cone angle for the spray liquid phase. In addition, Figure 4 shows sample spray images captured 0.2 ms after Start of Injection (aSOI) and in fully developed jet conditions for the analyzed duct configurations.

The duct insertion evidently influences the spray global shape evolution. Considering the free spray (red) as a reference, the spray tip penetration (Figure 3, left) is significantly enhanced by the standard configuration (blue), with a more moderate effect with the short design (same stand-off distance but reduced duct length, green). Shifting downstream the duct inlet section so to obtain the shifted duct (magenta) results in an initially reduced penetration at the timing of

TABLE 1 Analyzed duct configurations.

Configuration	*L* [mm]	*D* [mm]	*G* [mm]
Standard duct	14	2	2
Shifted duct	12	2	4
Short duct	10	2	2

© Politecnico di Torino

Downloaded from SAE International by Torino Politecnico, Tuesday, September 28, 2021

FIGURE 3 Spray tip penetration (left) and cone angle (right)—liquid phase. Operating conditions: vessel pressure = 20 bar; vessel temperature = 773 K; rail pressure = 1200 bar; energizing time = 1 ms.

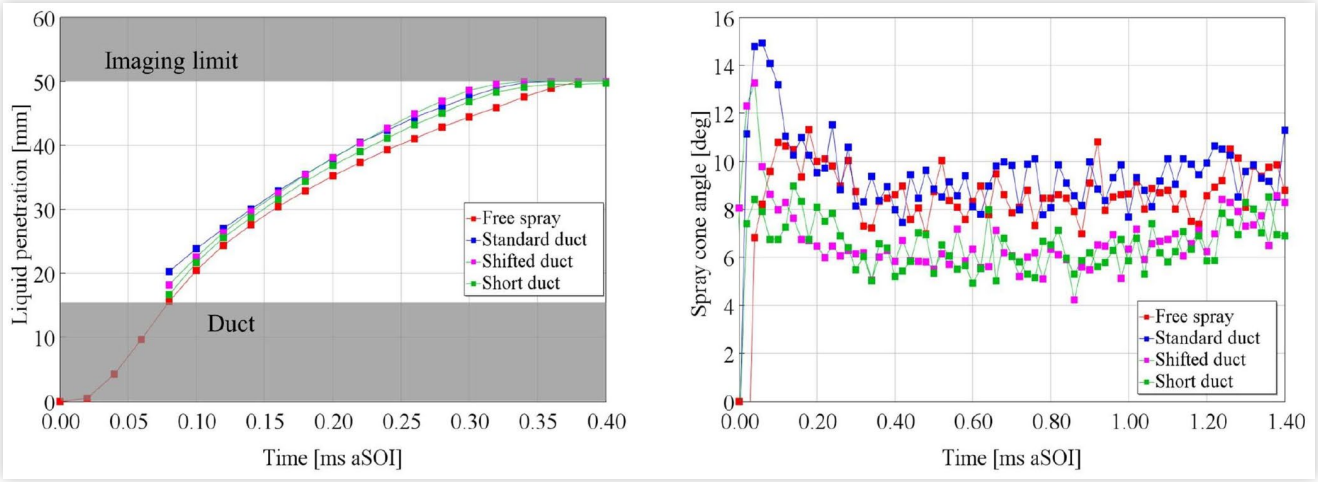

© Politecnico di Torino

the first appearance of the spray tip downstream the duct (80 μs aSOI), followed by an increased tip velocity in the following spray evolution with respect to the standard design. In other words, a significant reduction of the duct length (short vs standard duct) results in a drastic reduction of the duct effect, while shifting the duct inlet section with a moderate length reduction (shifted vs standard duct), the duct effect seems to be delayed and shifted downstream. In terms of spray cone angle (Figure 3, right), the insertion of the standard duct does not seem to affect the spray evolution to a large extent, at high vessel temperature, while a slight cone angle decrease was observed for both the shifted and the short configurations. The relevance of small differences in the duct design can be better perceived by observing the fully developed spray appearance (Figure 4, bottom). At the considered timing, the standard duct spray is completely different from the free-spray structure: the inner liquid core (dark in the image) is significantly less extended and compact, suggesting a more intense evaporation process. Around the spray tip, large blobs of liquid fuel periodically seem to detach from the main spray structure being dissolved downstream, thus defining a region where the fuel is vaporized over the entire plume section (Complete Vaporization Distance); for standard duct configuration, this distance is around 50 mm for the entire injection process duration. Conversely, with the shifted duct the complete vaporization takes place well downstream the 50 mm observation window. Finally, for the short duct configuration, the complete vaporization distance seems to be intermediate among the standard duct configuration and the shifted one: the geometrical inlet pattern for the spray and airstreams is the same as the standard duct, while the sucking driving force produced by the spray evolution in the duct could be less effective, as explained in the numerical section.

FIGURE 4 Spray global shape for free spray, standard duct, shifted duct, and short duct at 0.2 ms (top) and 1.0 ms (bottom) aSOI. Operating conditions: vessel pressure = 20 bar; vessel temperature = 773 K; rail pressure = 1200 bar; energizing time = 1 ms.

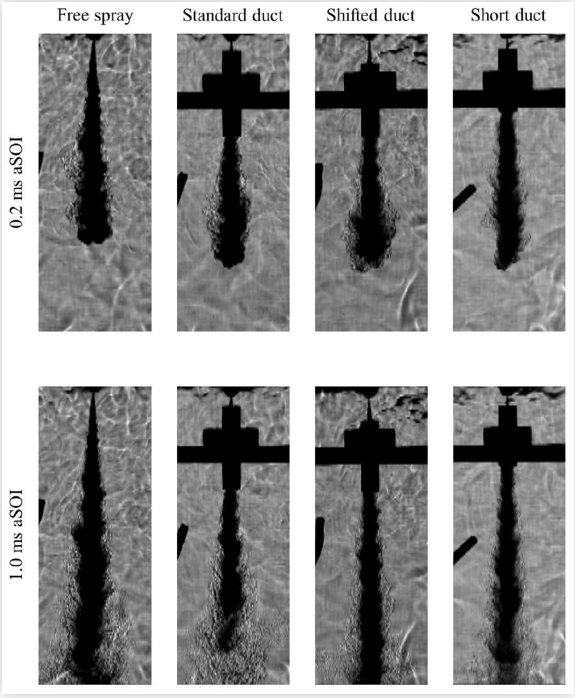

© Politecnico di Torino

2.2. Simulation Setup

In [25], a 3D-CFD spray model was developed in the commercially available software CONVERGE CFD [28] in order to investigate DFI with respect to free-spray evolution. The same model has been employed for the herein parametric analysis of DFI. The experimental CVV was reproduced in the virtual environment, and the duct temperature was assumed equal to the CVV one. The inner volume of the vessel was initialized

Downloaded from SAE International by Torino Politecnico, Tuesday, September 28, 2021

TABLE 2 Overview of the non-reacting 3D-CFD spray model setup.

Turbulence model	RANS – RNG k-ε [29]
Liquid injection	Blob model [30]
Droplet turbulent dispersion	O'Rourke model [31]
Spray breakup	KH-RT model [32]
Evaporation	Frossling with boiling model [31]
Droplet drag	Dynamic drop drag [33]
Spray/wall interaction	Rebound/Slide model [34]
Heat transfer	O'Rourke and Amsden model [35]

© Politecnico di Torino

reproducing the stationary experimental conditions before the injection event.

As far as the grid is concerned, the CVV volume was meshed with a patented cut-cell technique, fixing the base grid size equal to 2 mm. Two additional grid refinement cylindrical regions, centered along the spray axis, were added in the spray zone for the whole length of the experimental optical access window (diameter equal to 32 mm) and inside the duct, characterized by a minimum grid size of 0.5 mm and 0.25 mm, respectively. Furthermore, the Adaptive Mesh Refinement algorithm was activated to automatically refine the mesh where the flow field is under-resolved, dynamically as the solution changes, reaching a minimum cell size of 0.25 mm. Hence, Reynolds-averaged Navier-Stokes (RANS)-based non-reacting spray simulations were carried out, modeling liquid injection, primary and secondary breakup, drop drag, drop evaporation, droplet turbulence dispersion, drop/wall interaction, and heat transfer. The 3D-CFD spray model setup is summarized in Table 2.

The sub-models were accurately calibrated in order to reproduce the experimental data for both free-spray and DFI configurations on a large number of test cases, varying rail pressure, vessel pressure, and vessel temperature [25]. Subsequently, the model was employed for fully predictive combustion simulations, proving to be qualitatively in agreement with the results of the related scientific literature [14], in terms of the combustion process (e.g., ignition delay, combustion duration, combustion intensity) and soot emissions reduction. The combustion simulation setup featured the SAGE detailed chemistry solver with the Skeletal Zeuch chemical mechanism based on the n-heptane oxidation scheme [36], complemented by additional soot reactions from Mauss's work [37]: it globally consists of 121 species and 593 reactions. Given the strictly soot-related purpose of the work, the detailed Particulate Mimic model [38] was enabled through the inclusion of Polycyclic Aromatic Hydrocarbons (PAHs) as soot precursors.

2.3. Spray Model Validation

First of all, a further spray validation against the experimental data was carried out. Figure 5 shows the liquid penetration comparison between free-spray and DFI configurations for the three different duct geometries highlighted in Table 1, at vessel pressure = 20 bar, vessel temperature = 773 K, and rail pressure = 1200 bar operating condition. The spray model is able to replicate the experimental spray evolution with a more than satisfactory accuracy in the prediction of the liquid penetration for the tested duct geometries.

More specifically, in Figure 5, the standard duct outcome (blue) is compared with the shifted duct (magenta) on the left, and with the short duct (green) on the right. Starting from Figure 5 (left), standard duct and shifted duct show a similar

FIGURE 5 Liquid penetration curves for standard duct (blue) and shifted duct (magenta) configurations on the left and for standard duct (blue) and short duct (green) configurations on the right: comparison between numerical results (solid lines) and experimental data (square dots). Operating conditions: vessel pressure = 20 bar; vessel temperature = 773 K; rail pressure = 1200 bar.

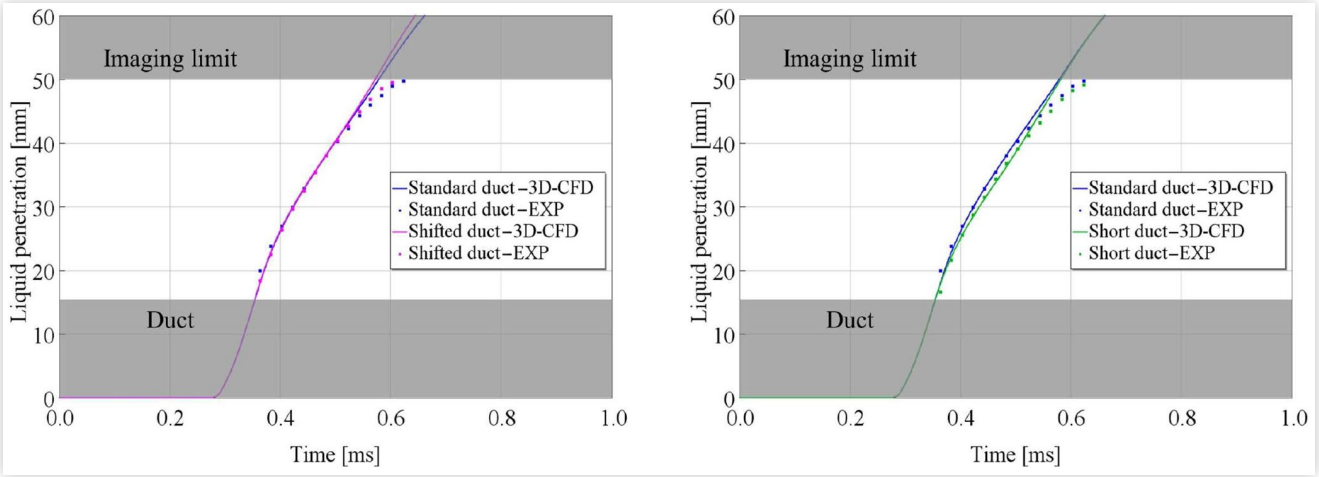

© Politecnico di Torino

Downloaded from SAE International by Torino Politecnico, Tuesday, September 28, 2021

penetration, thus confirming that the liquid spray evolution is not remarkably affected by the different entrance distances. In addition, the developed spray model can correctly predict the experimental spray behavior. Moving to Figure 5(right), as already highlighted, the short duct shows a lower spray velocity with respect to the standard duct. This result is also visible in the numerical simulation outcomes, confirming the high predictive capabilities of the calibrated spray model. Given the good agreement between available experimental data and simulation results varying both operating conditions [25] and duct geometry, the spray model was considered robust enough for parametric analysis of DFI toward a preliminary geometrical optimization.

3. Duct Geometry Numerical Optimization

The simulation activity was carried out with the purpose of understanding the influence of the main duct geometrical features on the ducted spray characteristics and on the combustion and soot emissions formation processes. With this aim, the DFI spray was analyzed in both non-reacting and reacting conditions, varying consecutively the following geometrical features:

- Stand-off distance (G) and duct length (L)
- Duct diameter (D)
- Duct inlet and outlet shape (Figure 6)

The *sharp duct* is the simplest configuration featuring a sharp inlet and outlet. This is the reference geometry for the herein study; thus, if not indicated differently, the duct must be intended as sharp. When the inlet shape is modified with a 45°-chamfer along the whole duct thickness, the duct shape is defined as *blunt duct*; while, when the outlet shape is characterized by a convergent outer diameter (configuration already studied in [14, 21]), the duct shape is defined as *tapered duct*. Moving to the different duct geometries evaluated, firstly, the G and L effect was analyzed by means of a Design of Experiments (DoE) technique keeping D equal to 2 mm. As a result, a full-factorial nine-element matrix was enlarged to cover two additional combinations of G and L representative of extremely low G and L values (i.e., G = 0.1 mm; L = 8 mm). The whole $G \times L$ matrix is highlighted with red dots in Figure 7. Afterward, the duct diameter was varied around the optimal combinations of the stand-off distance and duct length ranging between 1.5 mm and 3 mm, as shown by the black dots in Figure 7. Finally, *blunt* and *tapered* duct configurations (triangle and circle in Figure 7, respectively) were tested on the optimal (D, L, G) combination. A total of 23 different duct geometries were analyzed, and a simple naming convention was established as follows: D <diameter> L <length> G <stand-off distance>.

As already pointed out, each duct geometry was tested in both non-reacting and reacting conditions. On one side, non-reacting simulations had the aim of understanding the influence on air entrainment into the fuel spray and turbulent mixing without taking into account further effects derived from the combustion process. On the other side, both the analysis of the influence of the combustion process on the air entrainment and mixing, and the quantification of LOL and soot formation were evaluated through simulations in reacting conditions. The operating conditions of both the non-reacting and reacting simulations are reported in Table 3.

FIGURE 6 Tested duct shapes and fundamental duct geometric parameters (D, L, and G).

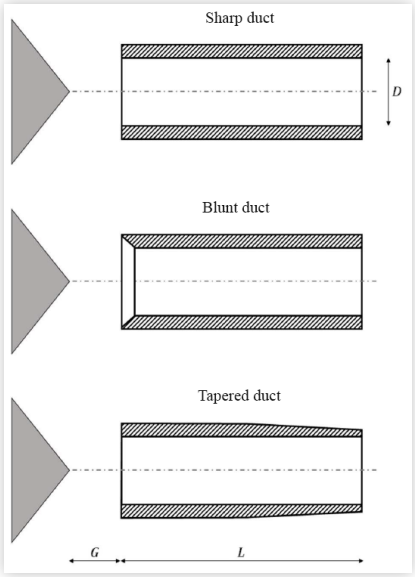

© Politecnico di Torino

FIGURE 7 Matrix of the tested duct geometries: $G \times L$ DoE matrix (red dots), D-sweep (black dots), blunt inlet shape (circle), and tapered outlet shape (triangle).

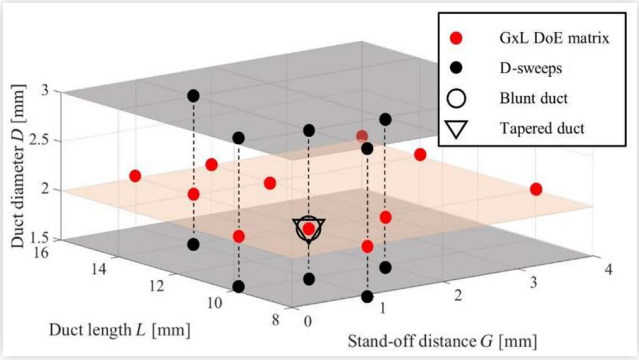

© Politecnico di Torino

TABLE 3 Non-reacting and reacting operating conditions.

Simulation phase	Vessel pressure [bar]	Vessel temperature [K]	Rail pressure [bar]
Non-reacting	20.0	773	1200
Reacting	57.3	900	1200

© Politecnico di Torino

Downloaded from SAE International by Torino Politecnico, Tuesday, September 28, 2021

3.1. Effect of Stand-Off Distance and Duct Length

Non-reacting Spray Physical Analysis In [24, 25] enhanced upstream air entrainment and turbulent mixing were detected for the DFI using numerical modeling. More specifically, the high air entrainment at the duct inlet was related to the pressure drop inside the duct while the turbulent mixing was linked, on one hand, to a high strain rate inside the duct and, on the other hand, to the high-velocity gradient at the duct outlet between the incoming high-speed ducted spray and the quasi-stationary air chamber, thus creating local turbulent eddies near the duct sharp edges. The combination of the abovementioned phenomena resulted in a remarkable equivalence ratio reduction in the core of the jet with respect to the free spray. Starting from these outcomes, a detailed analysis on the upstream air entrainment was carried out for the $G \times L$ matrix at $D = 2$ mm, measuring the air mass flow rate ($\dot{m}_{air}$) across the spray isosurface at a properly set value of overall equivalence ratio (i.e., fuel-to-air ratio including fuel liquid phase), until the spray impinges the duct inner wall [25]. Given the asymptotic behavior of the phenomenon, the mass flow rate was calculated only at 0.3 ms aSOI, when pseudo-stationary conditions are reached inside the duct. The results are reported in Figure 8.

At constant duct diameter, the longer G and L, the higher the upstream air entrainment. In particular, the G parameter seems to have more influence with respect to L. To better analyze this aspect, the pressure distribution along the spray axis (Z) is reported in Figure 9 considering four different duct geometries (D2L10G1, D2L10G4, D2L16G1, D2L16G4). The pressure distribution is depicted at 0.3 ms aSOI when airflow stationary conditions are reached inside the duct. For the sake of clarity, the duct axial placement for each geometry is illustrated in Figure 9 (bottom). Taking the D2L10G1 geometry (red line) as a reference, it can be observed that a G increase (D2L10G4, blue line) causes a slightly lower minimum pressure and shifted along the axis according to the duct inlet location. On the other side, at constant G, an L increment leads to a more significant influence on the pressure drop (D2L16G1, green line). Moreover, as expected, the simultaneous variation of G and L (D2L16G4, magenta line) causes a combined effect on the pressure in terms of absolute drop value and its position along the duct axis.

The huge impact of duct length on the in-duct pressure drop could be explained considering the flow evolution within the duct. In the DFI configuration, the entraining air, driven by the jet momentum, increases its velocity since it is constrained to pass through a much smaller flow area with

FIGURE 8 Contour plot of the air entrainment into the fuel spray upstream the duct inlet as a function of G and L ($D = 2$ mm) at 0.3 ms aSOI. Operating conditions: vessel pressure = 20.0 bar; vessel temperature = 773 K; rail pressure = 1200 bar.

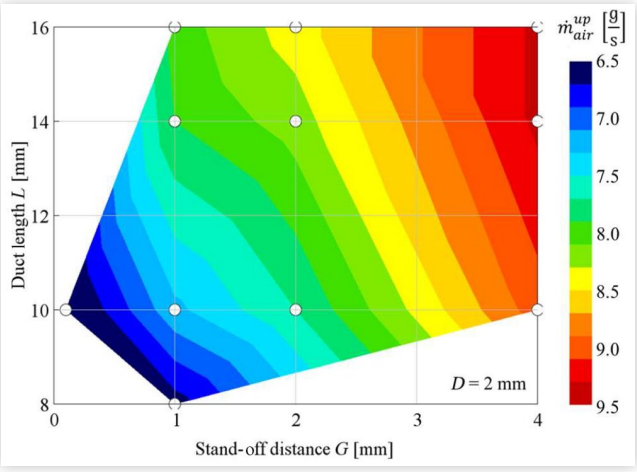

© Politecnico di Torino

FIGURE 9 Pressure evolution (top) along the Z-axis of the spray at 0.3 ms aSOI for the following duct geometries: D2L10G1 (red), D2L10G4 (blue), D2L16G1 (green), D2L16G4 (magenta). The location of the ducts for each configuration is illustrated at the bottom. Operating conditions: vessel pressure = 20.0 bar; vessel temperature = 773 K; rail pressure = 1200 bar.

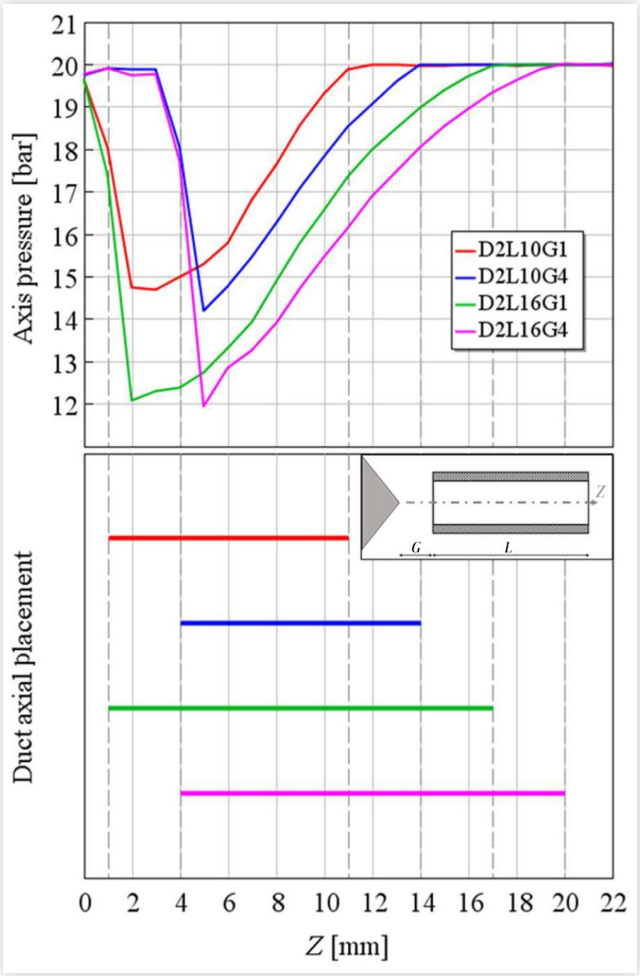

© Politecnico di Torino

Downloaded from SAE International by Torino Politecnico, Tuesday, September 28, 2021

respect to the free spray. According to the energy conservation, neglecting in first approximation the air density variations, the increase in kinetic energy is reached by means of a decrease in pressure energy; thus, the pressure inside the duct drops down. Thereby, the higher the duct length, the longer the space in which the pressure energy can be converted into kinetic energy before rising again for continuity reasons at the duct exit, where the pressure must be equal to the CVV condition.

However, the upstream air entrainment distribution (Figure 8) is not only a function of pressure drop in the duct volume but also of available minimum flow area. In fact, comparing the D2L10G4 (blue) and D2L16G1 (green) configurations in Figure 9, it can be easily visualized that the longer duct shows a much higher pressure variation with respect to the shorter geometry; however, the longer duct results in lower upstream air entrainment with respect to the configuration with short duct but with duct inlet location farther from the injector tip. In other words, the amount of upstream air entrainment depends not only on the static pressure stratification in the duct but also on the minimum flow area, A_{min}, highlighted in Figure 10, that is strictly dependent on the duct configuration (i.e., G, D, inlet shape).

As far as the G is concerned, since it linearly affects the minimum flow area, it has a strong influence on the upstream air entrainment. To quantify this dependency, Figure 11 shows the correlation between minimum flow area and upstream air entrainment, normalized with respect to the maximum, for the tested $G \times L$ matrix.

Once the geometry influence on the upstream air entrainment is assessed, the focus was moved to the enhanced turbulent mixing. In [25], this effect was decomposed in a two-stage process for DFI: on one hand, a highly turbulent regime is reached inside the duct due to the strong velocity gradients between the inner wall and the spray axis; on the other hand, the velocity gradient between the high-momentum jet and the surrounding quiescent air at the duct exit creates a vortex ring, which triggers a high turbulent zone downstream of the duct. To quantitatively evaluate the turbulent mixing, the maximum TKE value for each cross-section of the spray at 0.3 ms aSOI was selected as a turbulence index for the whole 3D TKE field. The TKE index is reported in Figure 12 (top) as a function of the spray axis, for the four different duct

FIGURE 10 Sketch of the minimum flow area for the upstream entraining mass flow rate ("Air flow").

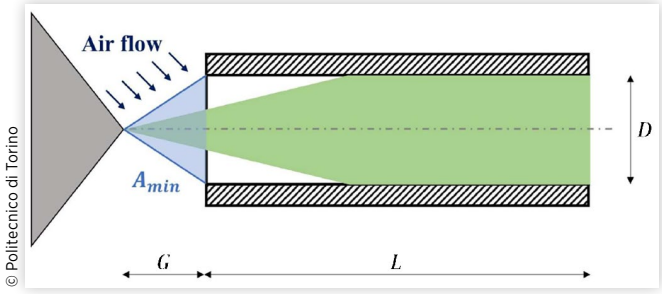

© Politecnico di Torino

FIGURE 11 Normalized upstream air entrainment as a function of normalized minimum flow area at different G at 0.3 ms aSOI. Operating conditions: vessel pressure = 20.0 bar; vessel temperature = 773 K; rail pressure = 1200 bar.

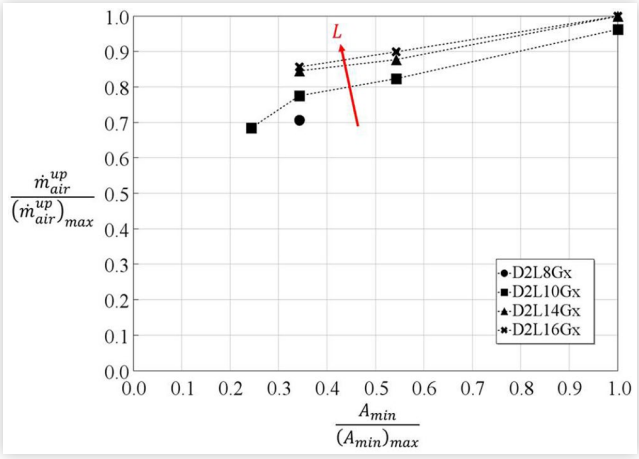

© Politecnico di Torino

geometries previously analyzed (Figure 9) and for the free-spray configuration for comparison purposes. Furthermore, the maximum equivalence ratio (ϕ_{max}) for each cross-section of the spray is also reported (Figure 12, middle) to directly evaluate the effect of turbulence on air/fuel mixing. It is worth noting that the maximum values instead of the average quantities were selected for both TKE and ϕ to avoid the noisy effect of evaporation and breakup processes on the mean quantities. In addition, with the aim of isolating the spray volume from the surrounding air in the CVV, the maximum values were computed only in a defined region by adopting an equivalence ratio filter to consider exclusively the computational cells in which $\phi > \phi_{threshold}$. As previously reported, Figure 12 (bottom) shows the duct axial placement for each geometry. Starting from the free-spray versus DFI comparison in terms of maximum TKE distribution (Figure 12, top), the abovementioned two stages of the mixing process can be clearly identified along the Z-axis. The first stage (i.e., in-duct turbulent regime) is evident by focusing on the TKE enhancement with respect to free spray (black) from the injector tip to the duct exit. This stage is characterized by a steep TKE increment at the beginning followed by a quasi-constant value characteristic of the geometry for a certain operating condition. In particular, this is verified for 3 geometries out of 4 (i.e., excluding the D2L10G1), in which a fully developed in-duct turbulent regime is established. Then, starting from the duct exit, the TKE significantly increases due to the high-velocity gradient (i.e., the second stage of the process). Evaluating in detail the different duct geometries, it can be concluded that the farther the duct exit from the injector tip, the higher the maximum TKE or, in other words, the second stage turbulent mixing retard is proportional to its intensity. This relation seems associated with the turbulence level reached inside the duct and with the related establishment of fully developed turbulent conditions at the duct exit. Indeed, the abovementioned D2L10G1 (red) geometry shows a remarkably lower

Downloaded from SAE International by Torino Politecnico, Tuesday, September 28, 2021

FIGURE 12 Maximum TKE (top) and maximum ϕ (middle) on the spray cross-section as a function of the *Z*-axis at 0.3 ms aSOI for the free-spray (black) and the following duct geometries: D2L10G1 (red); D2L10G4 (blue); D2L16G1 (green); D2L16G4 (magenta). The location of the ducts for each configuration is illustrated at the bottom. Operating conditions: vessel pressure = 20.0 bar; vessel temperature = 773 K; rail pressure = 1200 bar.

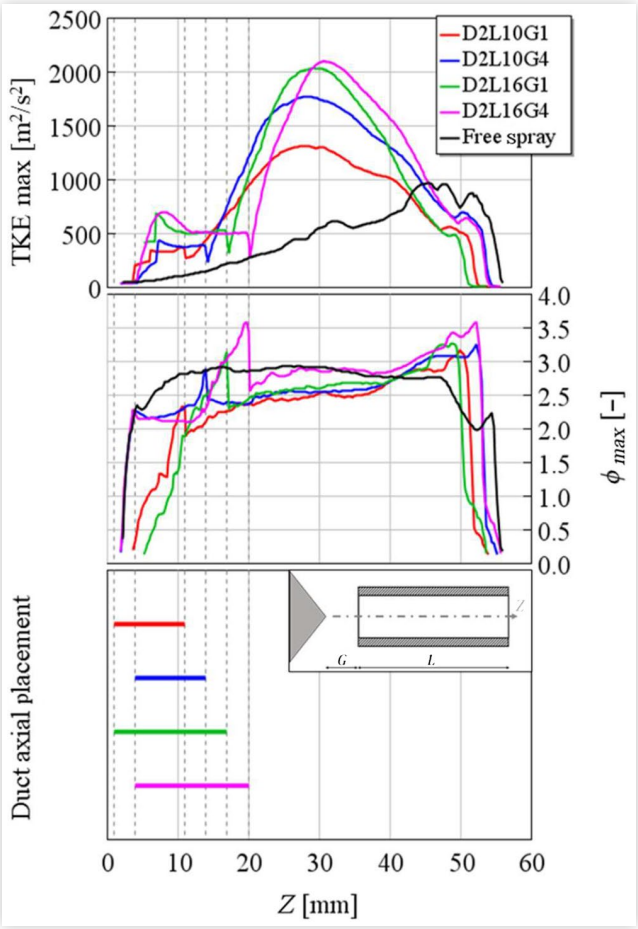

© Politecnico di Torino

TKE slope at the duct exit than the remaining three, whose maximum TKE intensity is comparable despite the further increment in duct exit location. Focusing on the equivalence ratio maximum (Figure 12, middle), it is noteworthy that each considered duct configuration shows more promising results in terms of air-fuel mixing than the free spray, for most of the spray domain. The analysis of the ϕ_{max} distribution (gas phase) needs to take into account the impact of the evaporation process especially in the region close to the injector tip. In fact, at constant duct length, the difference between the D2L10G1 (red) and D2L10G4 (blue) geometries can be attributed to the lower spray contact with the surrounding air, thus reducing the evaporation rate. The minimum ϕ_{max} after the duct exit is achieved with the duct geometry in which the second-stage turbulent mixing is advanced and therefore less intense (D2L10G1, red line), suggesting that the equivalence ratio reduction is a trade-off between the intensity and the timing of the mixing. In fact, the shorter the duct exit location, the higher the capability of the spray of entraining air downstream of the duct, which is totally inhibited along the duct collision length [19]. More specifically, although the turbulent mixing is enhanced inside the duct, the ϕ_{max} distribution close to the duct exit for the longest tested ducts (D2L16G1, green, and D2L16G4, magenta) rises more than the one obtained in free-spray configuration due to the steep increment along the duct collision length. In other words, the maximum turbulent mixing is not enough to determine the most effective duct geometry in reducing ϕ because the turbulent motion has to be combined with a sufficient amount of entraining air [23].

Combustion Analysis

In the analysis of the non-reacting phase, both the upstream entrained mass flow rate and the turbulent mixing have been identified as indexes of the effectiveness of a certain duct configuration in soot mitigation. However, both the mechanisms and the subsequent equivalence ratio can be remarkably affected when combustion is enabled, thus changing the optimal duct geometry. For the herein purposes, the LOL is used as an axial threshold to quantify the capability of a certain spray configuration (both free spray and DFI) in entraining air and mixing it with fuel vapors before the combustion zone. First of all, the stabilized LOL contour plot at 1.2 ms aSOI for each $G \times L$ combination is reported in Figure 13. As defined in the literature [39, 40], the LOL was evaluated using the OH* radicals concentration,

FIGURE 13 Contour plot of the LOL as a function of *G* and *L* (*D* = 2 mm) at 1.2 ms aSOI. Operating conditions: vessel pressure = 57.3 bar; vessel temperature = 900 K; rail pressure = 1200 bar.

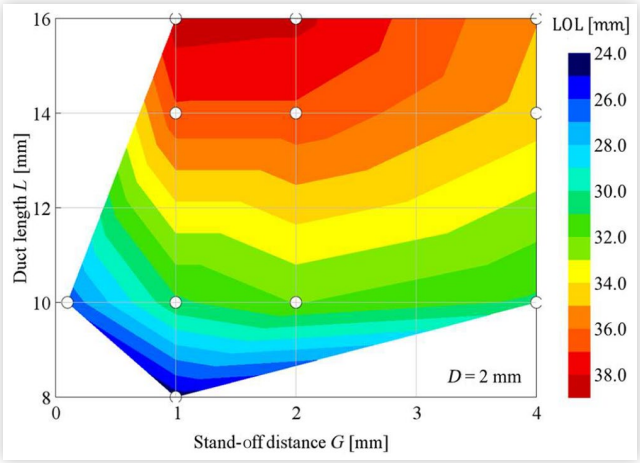

© Politecnico di Torino

Downloaded from SAE International by Torino Politecnico, Tuesday, September 28, 2021

FIGURE 14 Sketch of the isosurfaces for the calculation of the entraining mass flow rate ("Air flow") upstream and downstream of the duct in reacting conditions.

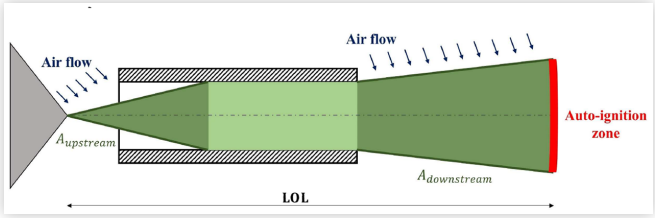

© Politecnico di Torino

identifying the computational cell closest to the injector tip overcoming a suitable OH* threshold.

It emerges that the LOL increases with the duct length due to the faster liquid penetration [21]. On the other side, the stand-off distance variation, which changes only the duct exit location keeping constant the axial spray confinement, leads to a maximum of the LOL for 1-2 mm value.

Once the LOL in reacting conditions is defined, the air entrainment was evaluated both upstream and downstream of the duct. The upstream airflow was computed as in the non-reacting simulation, while a similar methodology was adopted for the evaluation at the duct exit. In this case, the air mass flow rate was measured considering as cross-section of the isosurface at a ϕ value, properly set to contour the whole fuel spray in the axis range between the duct exit location and the LOL. A descriptive sketch of both the upstream and downstream isosurfaces, $A_{upstream}$ and $A_{downstream}$, is reported in Figure 14.

Since the upstream air entrainment is not affected by the combustion due to the large chamber volume, its contour plot is not reported. Same trends with G and L variations of non-reacting analysis were obtained (Figure 8) with the mass flow rate absolute values properly scaled due to the different CVV air density. The absolute downstream entrained mass flow rate, as well, is not here reported since it mainly depends on the net LOL (i.e., LOL minus collision length): the longer the net LOL, the higher the surface over which the mass flow rate is computed. In addition, the comparison between upstream and downstream air entrainment in terms of absolute values would have been misleading due to the difference in terms of flow area with $A_{downstream} > A_{upstream}$ for the evaluated duct geometries, thus not reflecting the real entrainment intensity. Therefore, the entrained mass flux was considered dividing the airflow per spray area unit. The upstream and downstream mass flux contour plots at 1.2 ms aSOI, when the airflow stationary conditions are reached, are reported in Figure 15 (left and right, respectively).

It is clear that the upstream entrainment mass flux is largely higher than the downstream one. This outcome is in line with Rhim et al.'s research work [41] that identifies the region close to the injector tip as the most relevant in terms of air entrainment intensity. Given that the Free Spray values (indicated in brackets in Figure 15) are much lower than DFI for the upstream entrainment mass flux while they are quite similar to DFI for the downstream one, it could be drawn that the duct adoption enhances the air entrainment where is most beneficial. As far as the geometry dependency is concerned, the upstream air-entrained mass flux shows a similar trend highlighted in non-reacting conditions (Figure 8), being $A_{upstream}$ not remarkably affected by the different CVV thermodynamic conditions and by the duct geometry variation. On the other side, the downstream air-entrained flux tends to grow reducing G and increasing L, highlighting its maximum with the D2L16G1 configuration.

Afterward, the turbulent mixing was evaluated considering the same methodology defined in non-reacting conditions for maximum TKE and equivalence ratio but reducing

FIGURE 15 Contour plots of the entrained mass flux into the fuel spray upstream (left) and downstream (right) of the duct as a function of G and L (D = 2 mm) at 1.2 ms aSOI. Operating conditions: vessel pressure = 57.3 bar; vessel temperature = 900 K; rail pressure = 1200 bar.

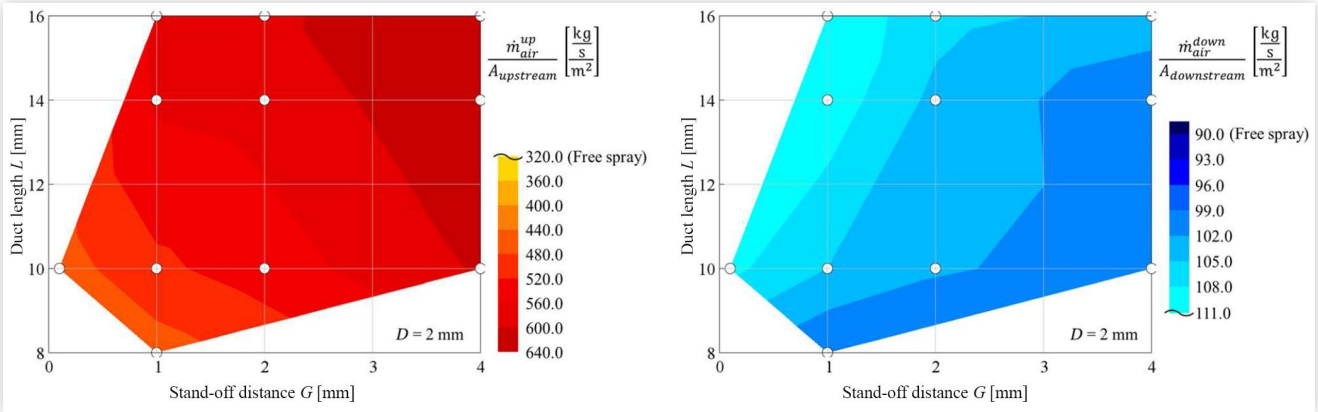

© Politecnico di Torino

Downloaded from SAE International by Torino Politecnico, Tuesday, September 28, 2021

FIGURE 16 Maximum TKE (top) and maximum ϕ (middle) on the spray cross-section as a function of the Z-axis at 1.2 ms aSOI for the following duct geometries: D2L10G1 (red); D2L10G4 (blue); D2L16G1 (green); D2L16G4 (magenta). The location of the ducts and the LOL are illustrated at the bottom. Operating conditions: vessel pressure = 57.3 bar; vessel temperature = 900 K; rail pressure = 1200 bar.

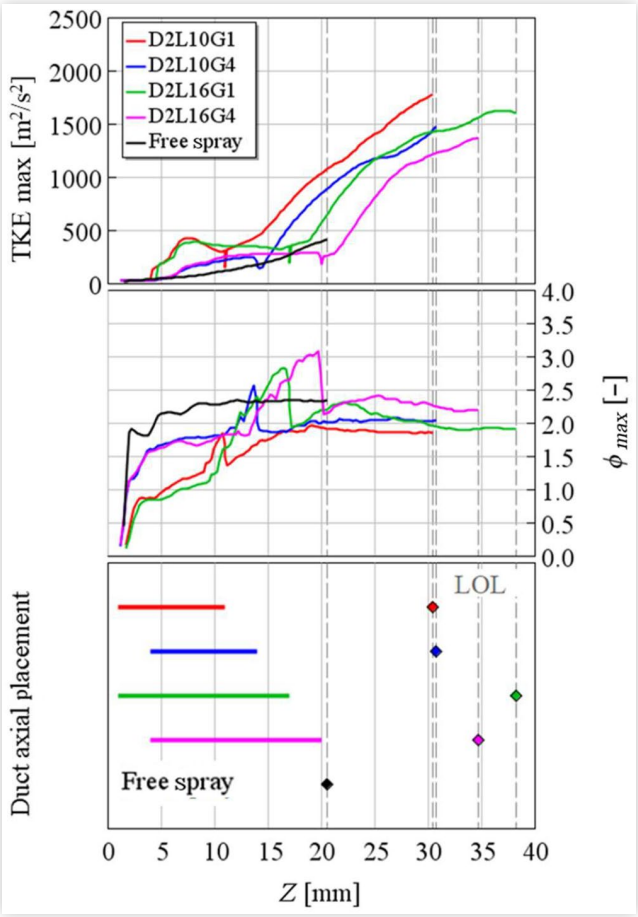

© Politecnico di Torino

the domain of interest at $0 < Z < \text{LOL}$. The maximum TKE and ϕ at 1.2 ms aSOI are depicted in Figure 16 (top and center, respectively) for the free-spray and the four different duct geometries already analyzed in the non-reacting analysis. In addition, the LOL is highlighted in Figure 16 (bottom), with a dashed line and indicators, in which the duct axial placement for each geometry is reported as well. As expected, the LOL plays a crucial role in determining the best balance between turbulent mixing and air entrainment since it is an index for both available time and spray surface for the air/fuel mixing. More in detail, taking the free spray as a reference, DFI geometries feature a definitely longer LOL, highlighting an increment of about 10-18 mm, depending on the duct configuration. On the other side, free-spray shows a maximum TKE lower than each DFI configuration for most of the analyzed domain, even considering a reduction of the gap between free-spray and in-duct TKE with respect to non-reacting simulation case (Figure 12, top). Lower turbulence and shorter LOL, highlighted in the free-spray configuration, lead to a not optimal air/fuel mixing, increasing the maximum ϕ at the LOL with respect to each duct geometry, as confirmed by Figure 16 (middle). Moving to the tested DFI configurations, several differences can be observed compared to the non-reacting simulations (Figure 12) concerning the maximum TKE (Figure 16, top): firstly, the in-duct TKE value is strongly dependent on the G value rather than the L; secondly, the second-stage turbulent mixing steep increment is less dependent on the duct exit location, showing a similar slope among the different duct geometries and making the timing more relevant. In reacting conditions, the distance between LOL and duct exit tends to be a controlling parameter for DFI turbulent mixing effectiveness. In fact, D2L10G1 (red) and D2L10G4 (blue) configurations show a similar TKE intensity at the duct exit, but the advanced duct exit location, at LOL approximately equal, guarantees higher TKE values for the D2L10G1 geometry. In other words, the duct geometry second-phase turbulent mixing capability has to be evaluated considering more than one aspect: the timing (i.e., duct exit location), the intensity (i.e., the slope), and the second-phase mixing length (i.e., LOL minus duct exit location). These considerations on maximum TKE, along with the evaluation of the abovementioned duct collision length, can be mirrored in the maximum ϕ distributions (Figure 16, middle). Indeed, the D2L10G1 geometry, which features the best turbulent mixing properties and the shorter collision length (due to the advanced duct exit), shows the lowest ϕ_{max} at the LOL and for most of the domain, apart from $Z < 12$ mm, where the higher D2L16G1 upstream air entrainment (Figure 15, left) prevails at similar evaporating conditions. Comparing the D2L10G4 and the D2L16G1, the latter shows a lower ϕ_{max} after the axial distance from the tip ($Z = 25$-30 mm) in which its maximum TKE value overcomes the former one. The difference is, then, enhanced due to the longer LOL. Finally, the D2L16G4 (magenta) geometry, characterized by the longest collision length and by the most retarded duct exit location, reduces the DFI potential in terms of ϕ_{max} reduction.

After the evaluation of the main soot mitigation mechanisms, the combustion process and soot emissions were evaluated with the aim of selecting the optimal combination of G and L for the operating conditions defined in Table 3. In Figure 17, the Heat Release Rate (HRR) and soot mass traces related to the free-spray and the already analyzed four duct geometries are reported. As far as the combustion process is concerned, DFI shows a retarded combustion start and, consequently, a more intense premixed combustion compared with free spray, confirming the results already available in the literature [13, 14]. Moreover, the impressive soot reduction achieved by the duct adoption is worth to be noted. More specifically, the D2L10G1 (red) geometry highlights the best performance in soot reduction due to the higher mixing rate at LOL enabled by a combination of a longer available mixing duration and higher turbulence, as highlighted in Figure 16.

The analysis concerning the soot mass was then extended to the whole $G \times L$ DoE matrix. The scalar soot mass ($Soot_{avg}$) was calculated as the integral of the time-dependent soot trace

Downloaded from SAE International by Torino Politecnico, Tuesday, September 28, 2021

FIGURE 17 HRR (top) and soot mass in the CVV (bottom) for the free-spray (black) and the following duct geometries: D2L10G1 (red); D2L10G4 (blue); D2L16G1 (green); D2L16G4 (magenta). Operating conditions: vessel pressure = 57.3 bar; vessel temperature = 900 K; rail pressure = 1200 bar.

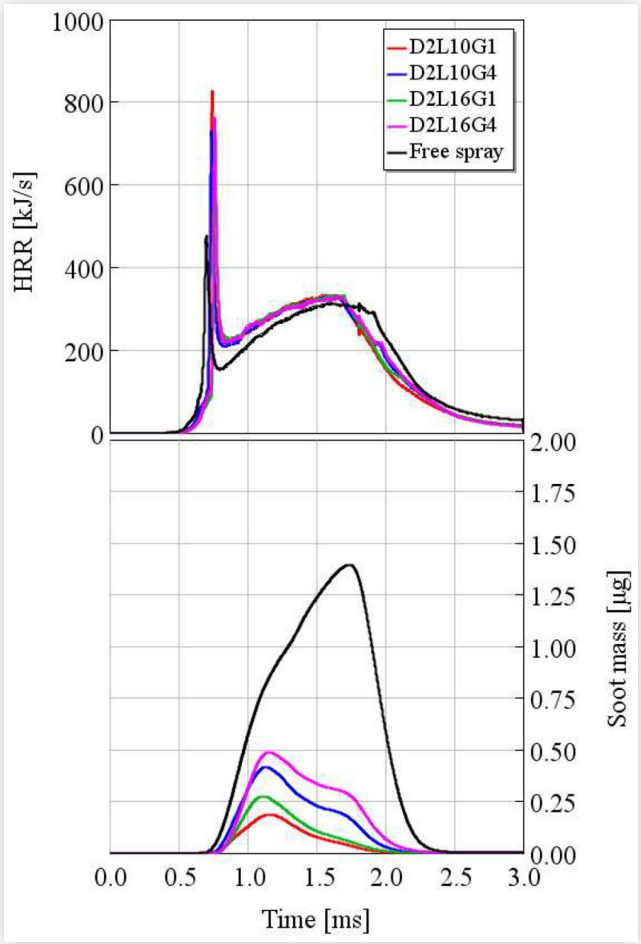

© Politecnico di Torino

FIGURE 18 Contour plot of the average soot mass in the CVV as a function of G and L (D = 2 mm) in the form of percentage reduction with respect to free spray. Operating conditions: vessel pressure = 57.3 bar; vessel temperature = 900 K; rail pressure = 1200 bar.

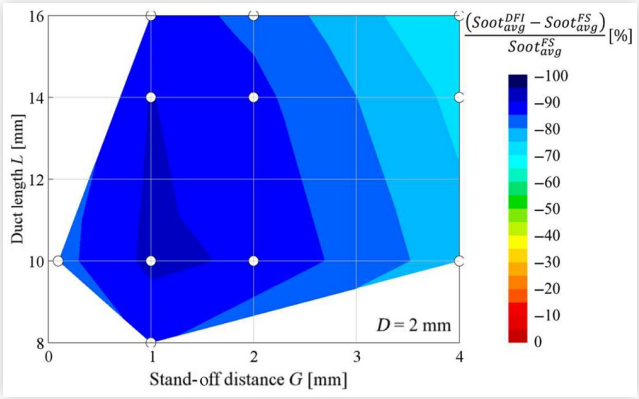

© Politecnico di Torino

divided for the injection duration (1.5 ms) and the contour plot of the soot mass percentage reduction with respect to free spray is reported in Figure 18.

As it can be clearly noted from Figure 18, the DFI confirms its remarkable soot formation mitigation potential; in fact, all the considered geometries show a drastic soot mass reduction of more than 70.0%. In particular, the D2L10G1 configuration allows the maximum soot attenuation achieving a reduction of 91.4% with respect to free spray. In conclusion, the optimal $G \times L$ combination is achieved by reducing the length of the duct and by placing it close to the injector tip until the air entrainment and LOL reductions overcome the benefits derived from the turbulent mixing. Indeed, taking the optimal configuration (D2L10G1) as a reference, the reduction of both L and G (8 mm and 0.1 mm, respectively) leads to a slightly higher soot mass due to the lower upstream air-entrained mass flux (Figure 15) and shorter LOL (Figure 13).

3.2. Effect of Duct Diameter

Non-reacting Spray Physical Analysis When the duct diameter varies according to the matrix in Figure 7(black dots), the air entrainment and mixing can drastically change. In Figure 19, from top to bottom, the upstream air entrainment, the maximum in-duct velocity, the minimum in-duct pressure, and the minimum flow area are reported at 0.3 ms aSOI (i.e., pseudo-stationary conditions reached inside the duct) as a function of the duct diameter, considering constant stand-off distance (G = 1 mm) and duct length (L = 10 mm).

Starting from Figure 19(b), the in-duct velocity is reduced, considering a larger duct cross-sectional area. Therefore, with a bigger duct diameter, the conversion from pressure energy to kinetic energy is reduced, causing a less-intense in-duct pressure drop as shown in Figure 19(c): for instance, D = 3 mm leads to about 2 bar of in-duct pressure reduction with respect to the CVV (20 bar), while a decrease of more than 8 bar is achieved with D = 1.5 mm. Nonetheless, this pressure variation is not directly reflected in the upstream air entrainment values (Figure 19(a)) which rises for a larger D. This is consistent with the already discussed outcomes: in fact, the pressure drop is one driver for the air entrainment enhancement in the duct along with the minimum flow area that acts as the control parameter for the mass flow rate since the increment in A_{min} (d) counterbalances the reduced pressure drop.

As far as the turbulent mixing is concerned, Figure 20 shows the cross-section maximum TKE (top) and maximum (middle) as a function of the Z-axis at 0.3 ms aSOI, considering the same duct configurations (D-sweep, G = 1 mm; L = 10 mm) and the free spray for comparison. At the bottom, the duct axial placement is reported highlighting the collision length with a gray line for each considered duct geometry.

As already pointed out, each considered duct configuration improves both TKE and air-fuel mixing with respect to

Downloaded from SAE International by Torino Politecnico, Tuesday, September 28, 2021

FIGURE 19 Upstream air entrainment (a), maximum velocity (b), and minimum pressure (c) on the *Z*-axis at 0.3 ms aSOI and entraining air minimum flow area (d) as a function of the duct diameter (*G* = 1 mm; *L* = 10 mm). Operating conditions: vessel pressure = 20.0 bar; vessel temperature = 773 K; rail pressure = 1200 bar.

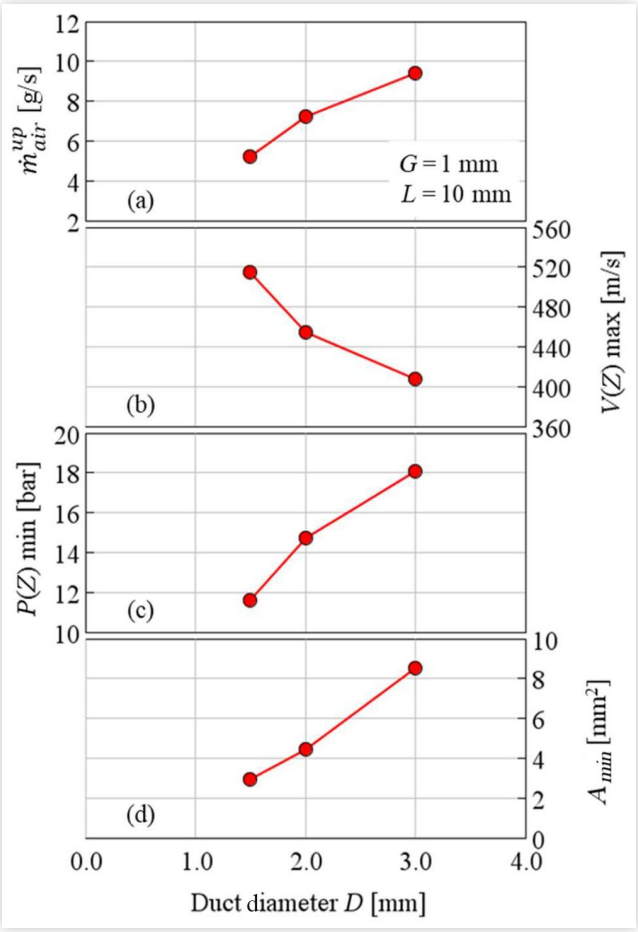

© Politecnico di Torino

FIGURE 20 Maximum TKE (top) and maximum ϕ (middle) on the spray cross-section as a function of the *Z*-axis of the spray at 0.3 ms aSOI for the free-spray (black) and the following duct geometries: D1.5L10G1 (cyan); D2L10G1 (red); D3L10G1 (yellow). The location of the ducts and the collision length (gray) are illustrated at the bottom. Operating conditions: vessel pressure = 20.0 bar; vessel temperature = 773 K; rail pressure = 1200 bar.

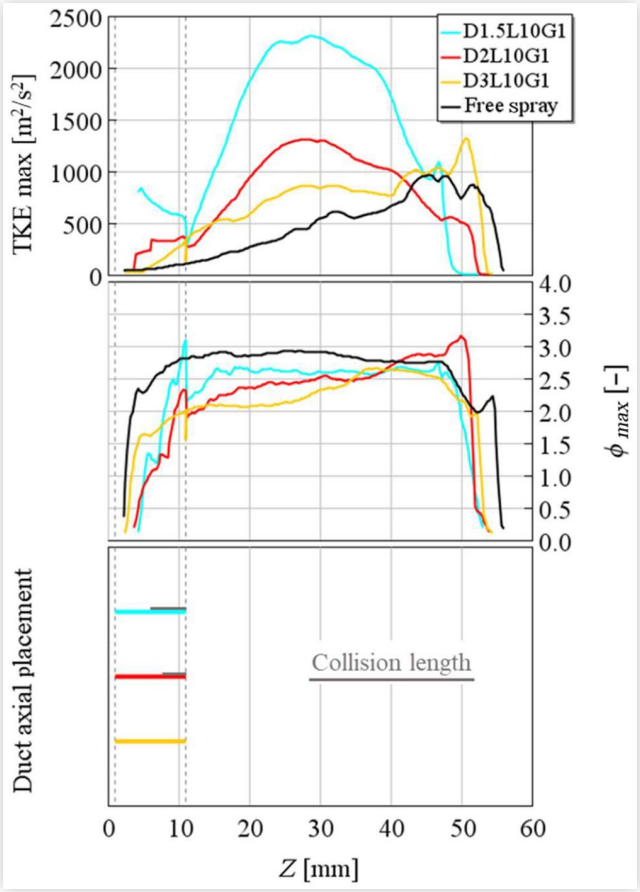

© Politecnico di Torino

the free spray. Focusing on the top graph, the in-duct maximum TKE is higher for the smallest diameter (D1.5L10G1, cyan), highlighting a dependency on the in-duct velocity, which increases the Reynolds number and, thus, the strength of the turbulent regime through the small pipe. Consequently, the higher in-duct spray velocity leads to a more intense second turbulent mixing phase since a larger amount of kinetic energy after the duct exit is dissipated in TKE. Moving to maximum ϕ distribution, it is noteworthy that the D3L10G1 does not show the steep increment close to the duct exit since the collision length, where the entrainment process is almost zeroed, tends to disappear. On the contrary, the D1.5L10G1 configuration even overcomes the free spray ϕ in that phase. From a general point of view, in non-reacting conditions the minimum ϕ is reached with the largest *D*, thus suggesting that the improved entrainment rate due to both flow area increment and collision length reduction influences more than the enhanced turbulence.

Combustion Analysis The combustion results, in terms of HRR and soot mass traces, for the same spray configurations already analyzed in Figure 20, are reported in Figure 21. Differently from the abovementioned results, the D3L10G1 duct (yellow) leads to a remarkable higher soot mass (Figure 21, bottom) not only with respect to the other duct geometries but also to the free spray (black). In particular, it features an average soot mass in the CVV throughout the combustion event about 1.2 times the free spray and even 13.6 times the D2L10G1 (red). On the other hand, the soot mass obtained with the D1.5L10G1 geometry (cyan) is significantly lower than the free spray, but more than twice with respect to the D2L10G1. This result is in line with the reduction of the

Downloaded from SAE International by Torino Politecnico, Tuesday, September 28, 2021

FIGURE 21 HRR (top) and soot mass in the CVV (bottom) as a function of time for the free-spray (black) and the following duct geometries: D1.5L10G1 (cyan); D2L10G1 (red); D3L10G1 (yellow). Operating conditions: vessel pressure = 57.3 bar; vessel temperature = 900 K; rail pressure = 1200 bar.

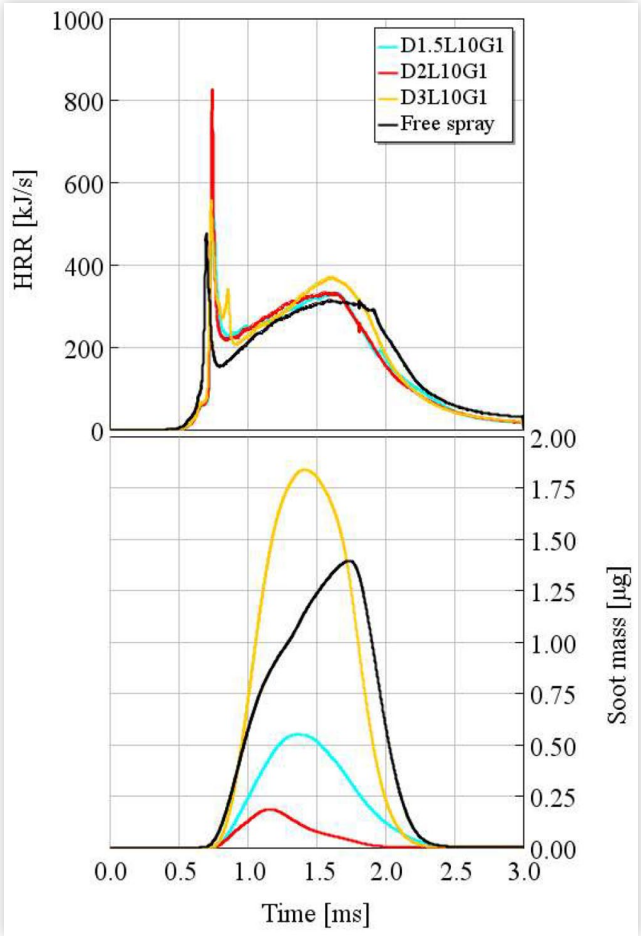

© Politecnico di Torino

FIGURE 22 Soot mass and temperature distribution on a section of the spray flame at 1.2 ms aSOI for the following duct geometries: D1.5L10G1 (top); D2L10G1 (middle); D3L10G1 (bottom). Operating conditions: vessel pressure = 57.3 bar; vessel temperature = 900 K; rail pressure = 1200 bar.

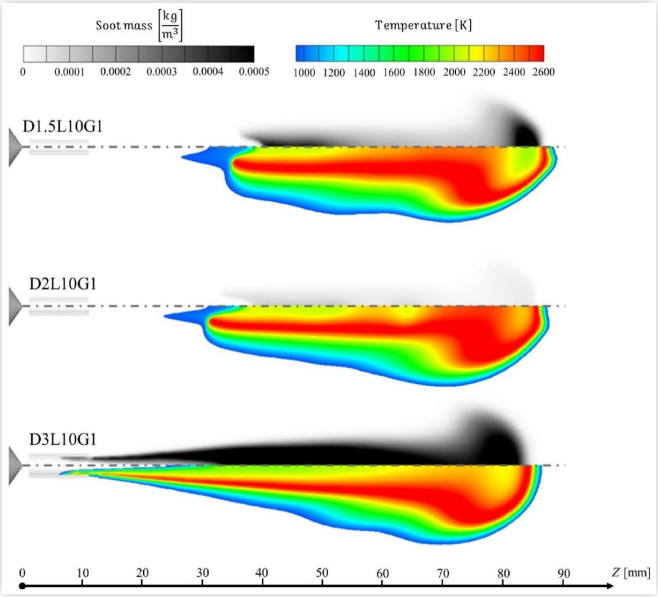

© Politecnico di Torino

upstream air entrainment (Figure 19(a)) which inhibits the soot formation mitigation process.

To better understand the soot mass outcomes in Figure 21, the temperature and soot distribution on a section of the spray flame for the three duct geometries at 1.2 ms aSOI are reported in Figure 22. Comparing D1.5L10G1 (top) and D2L10G1 (middle), it can be noticed the different soot mass distribution along the spray axis. More specifically, considering $Z < 70$ mm, the soot mass is slightly higher for the smallest diameter, confirming that the lower upstream air entrainment leads to higher soot formation, even considering the favorable effect of the longer LOL achieved with the reduced diameter. Focusing on the flame tip ($Z > 70$ mm), the temperature distribution differs: the smallest diameter leads to a temperature in the core of the spray tip below 2000 K, about 300 K lower than the D2L10G1 configuration, thus resulting in a lower oxidation capability. Increasing the duct diameter, D3L10G1 (bottom), the combustion starts within the duct volume as shown by the temperature contour plot, preventing any additional entrainment and mixing at the duct outlet, causing a remarkable soot increment. Furthermore, the premature combustion deteriorates both the first-stage turbulent mixing, due to the shorter in-duct mixing length linked to the LOL reduction, and the upstream air entrainment, due to the in-duct pressure rise given by combustion [26]. This result confirms the outcomes highlighted in [14], where the drawbacks associated with an in-duct combustion event were experimentally demonstrated.

A possible explanation of the in-duct combustion onset for the D3L10G1 geometry is illustrated in Figure 23, in which the pressure field, the liquid drops distribution, and the streamlines at the duct inlet and outlet on a spray longitudinal section are reported at 1.2 ms aSOI, for the previously shown three duct configurations.

As said before (Figure 19(c)), the in-duct pressure distributions are definitely affected by the duct diameter variation, but the in-duct pressure remains always lower than the CVV one. Focusing on Figure 23 (bottom), it can be observed that the collision length of the D3L10G1 case tends to zero; thus the expected DFI dynamic changes, being absent the spray/wall interaction. In particular, the gap between spray and wall at the duct outlet leads to a reverse airflow pumped downstream of the duct. This backflow causes the formation of some eddies inside the duct, leading to the stagnation of fuel vapors which, once depleted the ignition delay, burn and establish a spray flame starting upstream of the duct exit.

In Figure 24, the scalar soot mass $G \times L$ contour plots are reported for $D = 1.5$ mm, $D = 2$ mm (zoomed in from

Downloaded from SAE International by Torino Politecnico, Tuesday, September 28, 2021

FIGURE 23 Pressure field, liquid drops distribution, and streamlines at duct inlet and outlet on a section of the spray at 1.2 ms aSOI for the following duct geometries: D1.5L10G1 (top); D2L10G1 (middle); D3L10G1 (bottom). Operating conditions: vessel pressure = 57.3 bar; vessel temperature = 900 K; rail pressure = 1200 bar.

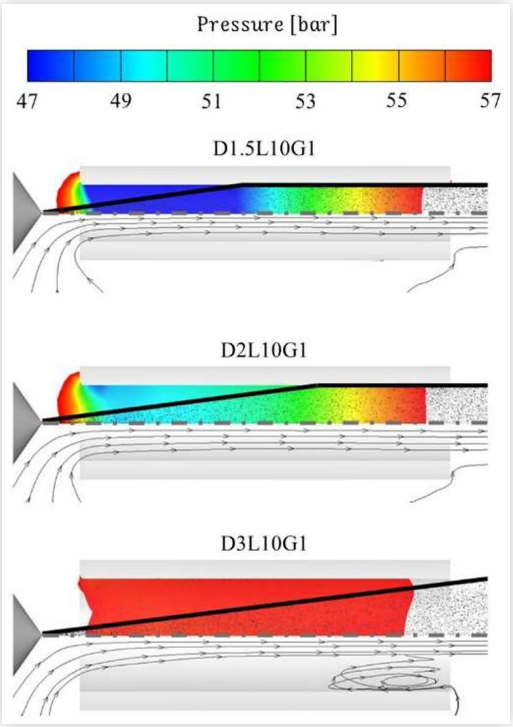

© Politecnico di Torino

Figure 18), and $D = 3$ mm in the form of percentage reduction with respect to free spray.

Starting from $D = 1.5$ mm (Figure 24, left), although the soot reduction is less pronounced than the $D = 2$ mm configuration (Figure 24, middle), DFI remains effective in breaking down the soot formation, leading to an average soot mass reduction of more than 40% for each duct configuration. As for the whole $D = 2$ mm contour plot (Figure 18), DFI becomes more effective in reducing G (until the upstream air entrainment starts to drastically reduce) and L (to advance the turbulent mixing and the air entrainment downstream of the duct). In this case, the optimal configuration features $L = 8$ mm reaching approximately 80% of soot mass reduction with respect to free spray. Focusing on the $D = 3$ mm case (Figure 24, right), 3 configurations out of 5, featuring $L = 10$ mm, show the combustion event inside the duct volume. As already pointed out, the DFI entrainment and mixing benefits are lost leading to an overall air-fuel mixing process worse than the free-spray configuration. Varying L, DFI is again effective in reducing soot emission, with an abatement of about 80% for $L = 8$ mm configuration, and 60% for $L = 14$ mm. Referring to Figure 23, the former case even further prevents the collision length establishment, manifesting that DFI could also work without spray/wall interaction; the latter instead newly establishes the collision length due to the longer L and DFI can work as expected.

3.3. Effect of Duct Shape: Blunt Inlet and Tapered Outlet

Non-reacting Spray Physical Analysis Different inlet (blunt duct) and outlet (tapered duct) geometries were tested exclusively on the optimal duct configuration of previous results based on a sharp geometry (i.e., D2L10G1). The upstream air entrainment results at 0.3 ms aSOI for the three analyzed duct shapes are reported in the bar chart in Figure 25. The *blunt duct* improves the air entrainment upstream of the duct by about 6% with respect to the *sharp*

FIGURE 24 Contour plots of the average soot mass in the CVV as a function of G and L in the form of percentage reduction with respect to free spray for ducts with $D = 1.5$ mm (left), $D = 2$ mm (middle), and $D = 3$ mm (right). Operating conditions: vessel pressure = 57.3 bar; vessel temperature = 900 K; rail pressure = 1200 bar.

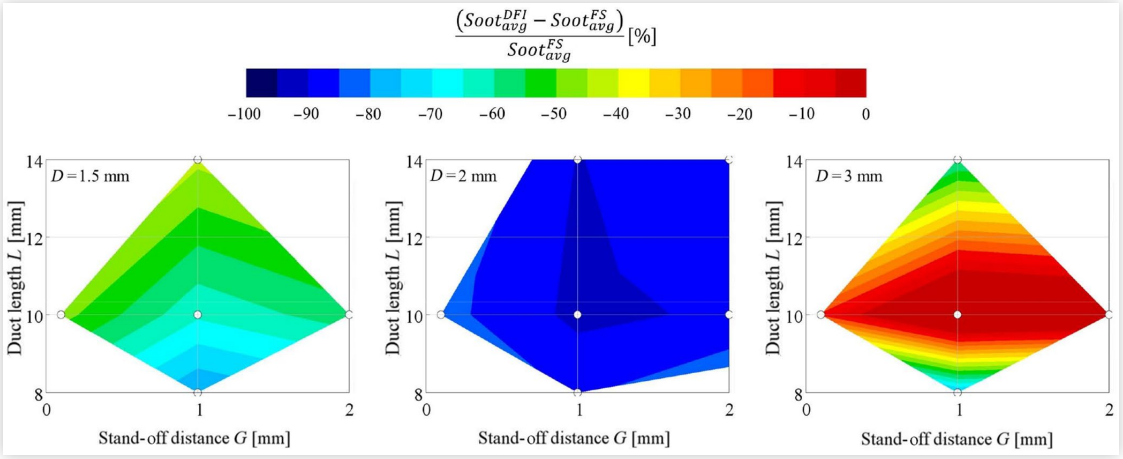

© Politecnico di Torino

Downloaded from SAE International by Torino Politecnico, Tuesday, September 28, 2021

FIGURE 25 Upstream air entrainment at 0.3 ms aSOI for three different duct shapes (D2L10G1 geometry), defined in Figure 6: sharp duct (left), blunt duct (middle), tapered duct (right). Operating conditions: vessel pressure = 20.0 bar; vessel temperature = 773 K; rail pressure = 1200 bar.

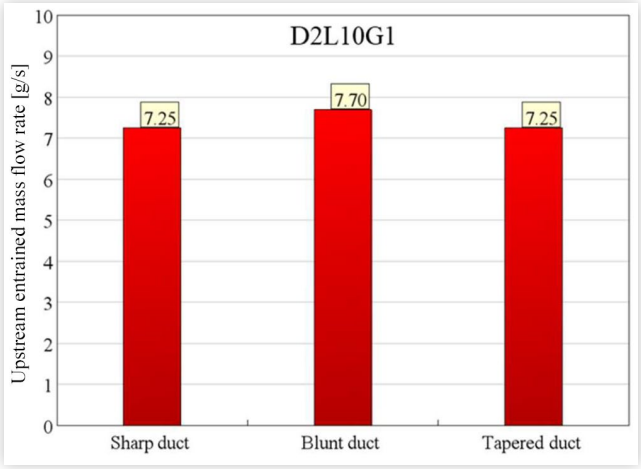

© Politecnico di Torino

duct, while the *tapered duct* does not affect it at all, as expected. In particular, the blunt inlet shape does not significantly change the in-duct pressure distribution but, on one hand, increases the minimum flow section and, on the other hand, improves the incoming flow directionality. As far as the turbulent mixing is concerned, no substantial differences were detected in non-reacting conditions changing the duct shape; thus, the results are not reported.

Combustion Analysis The LOL and the maximum and average ϕ at LOL at 1.2 ms aSOI are reported in Figure 26 to evaluate the three duct shapes in reacting conditions.

Starting from Figure 26 (top), the *blunt duct* geometry extends the LOL with respect to the other two, thereby improving the downstream air entrainment as well (Figure 26, bottom). On the other side, the *tapered duct* features no significant variation with respect to the *sharp* one.

To evaluate the effect of the different ϕ at LOL caused by the duct geometry modification, the HRR and soot mass traces related to the three duct shapes and free spray are reported in Figure 27.

Even if the HRR traces (Figure 27, top) are practically overlapped for each duct configuration, some differences can be highlighted in terms of soot (Figure 27, bottom). Because of the higher upstream air entrainment, the extended LOL and the consequent ϕ reduction, the *blunt duct* (red, dotted line) leads to a further improvement in soot mitigation with respect to the *sharp duct* (red, continuous line), reaching 94% of average soot mass reduction in comparison with conventional injection. On the contrary, the *tapered duct* (red, dashed line) does not significantly modify the results already obtained with the sharp shape.

FIGURE 26 LOL (top) and equivalence ratio (bottom) at the LOL at 1.2 ms aSOI for three different duct shapes (D2L10G1 geometry), defined in Figure 6: sharp duct (left), blunt duct (middle), tapered duct (right). Both maximum (red) and average (gray) equivalence ratios are illustrated. Operating conditions: vessel pressure = 57.3 bar; vessel temperature = 900 K; rail pressure = 1200 bar.

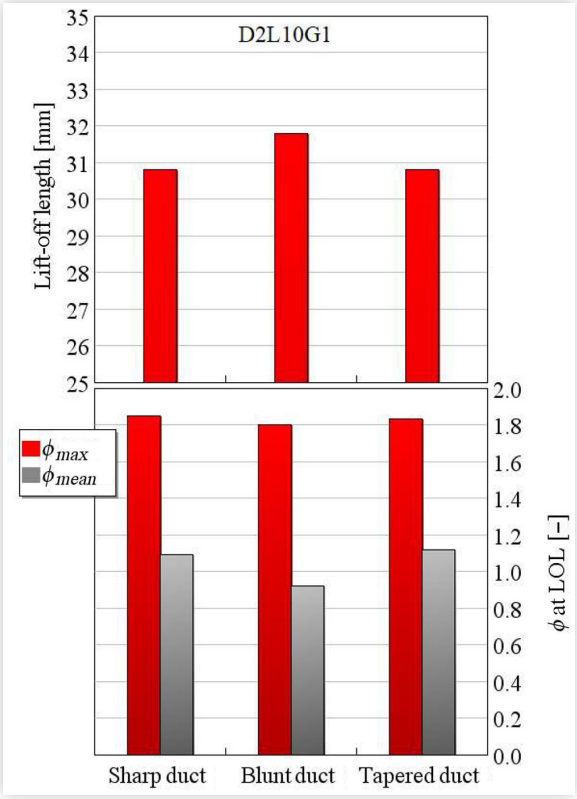

© Politecnico di Torino

3.4. Free-Spray versus Optimal DFI Configuration

A comparison between free-spray and optimal DFI configuration (D2L10G1, *Blunt*) in terms of equivalence ratio and TKE distribution on a spray longitudinal section in non-reacting conditions is reported in Figure 28. Looking at the bottom side of each spray, DFI features a significant TKE enhancement not only inside the duct volume but also downstream of the duct exit in which the established high recirculating turbulent mixing zone more than doubles the TKE with respect to the free spray. Moving to the top side of each spray, DFI strongly affects the equivalence ratio distribution inside the duct: on one hand, the upstream air entrainment (improved through the chamfer at the duct inlet) reduces the maximum value reached; on the other hand, the higher mixing leads to an overall homogeneity, also avoiding the radial ϕ distribution typical of the free spray. The relatively

Downloaded from SAE International by Torino Politecnico, Tuesday, September 28, 2021

FIGURE 27 HRR (top) and soot mass in the CVV (bottom) as a function of time for the free-spray (black) and three different duct shapes (D2L10G1 geometry), defined in Figure 6: sharp duct (red, continuous line), blunt duct (red, dotted line), tapered duct (red, dashed line). Operating conditions: vessel pressure = 57.3 bar; vessel temperature = 900 K; rail pressure = 1200 bar.

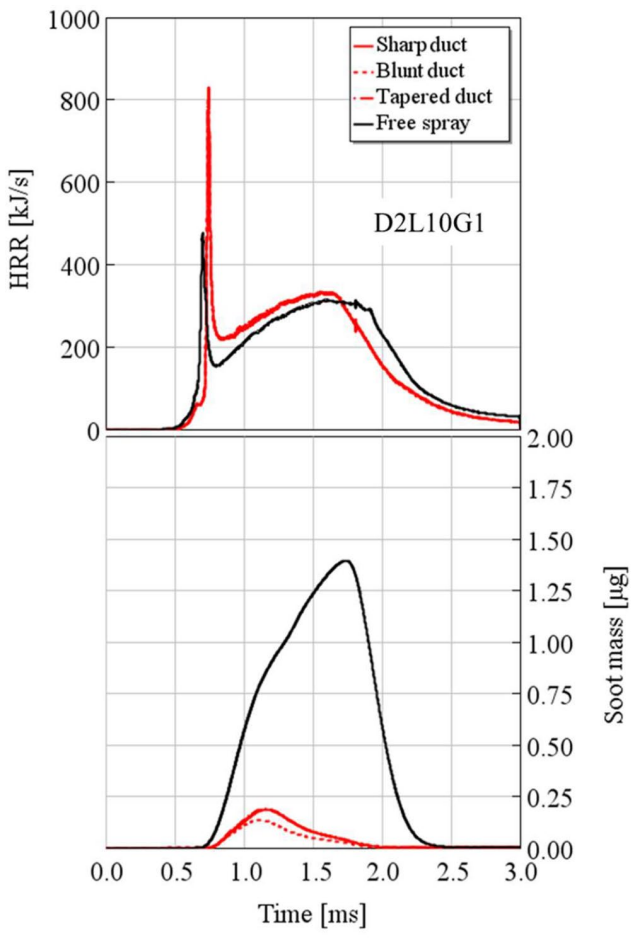

© Politecnico di Torino

FIGURE 28 Equivalence ratio and TKE distribution on a section of the spray at 0.7 ms aSOI for free-spray (top) and DFI (bottom) featuring the optimized duct configuration (D = 2 mm; L = 10 mm; G = 1 mm; blunt inlet). Operating conditions: vessel pressure = 20.0 bar; vessel temperature = 773 K; rail pressure = 1200 bar.

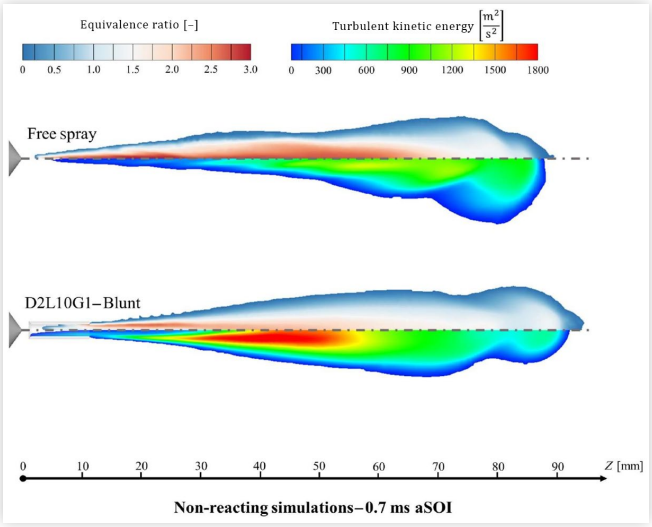

© Politecnico di Torino

short collision length of this duct geometry limits the drawbacks on the equivalence ratio associated with the temporary air entrainment inhibition. At the duct exit, the second turbulent mixing phase continues to homogenize the equivalence ratio field, leading to much lower ϕ values than free spray.

In Figure 29, a comparison between free-spray and optimal DFI configuration (D2L10G1-*Blunt*) in terms of temperature and soot distribution on a section of the flame is reported. By using this duct geometry, DFI features a definitely longer LOL, a more compact and high-temperature flame, which allows almost zero-soot diesel combustion compared to the high-soot free-spray flame.

4. Conclusions

The present work aimed to understand the influence of the main parameters of duct geometry on the DFI spray characteristics and on the combustion and soot formation processes. A previously developed 3D-CFD spray model was further validated in non-reacting conditions against new liquid penetration experimental data showing good predictive capability even when duct geometry is varied. This model was thus employed for an extensive investigation of the main duct geometrical features (stand-off distance G, duct length L, duct diameter D, and inlet/outlet shape) effect in both non-reacting and reacting conditions.

The DFI soot formation mitigation depends on a lower and more homogeneous equivalence ratio in the autoignition zone. The air entrainment upstream of the duct and the turbulent mixing after the duct exit are the main drivers of this achievement. In particular, the former depends on the pressure drop inside the duct and on the available minimum flow area for the entraining air, while the latter is influenced by the timing of occurrence (i.e., the duct exit location), the turbulence intensity (i.e., the extent of the rapid increase of its values), and the mixing length (i.e., the distance between duct exit and LOL). All these aspects are extremely affected by the abovementioned duct geometrical features and the main

Downloaded from SAE International by Torino Politecnico, Tuesday, September 28, 2021

FIGURE 29 Soot mass and temperature distribution on a section of the spray flame at 1.2 ms aSOI for free spray (top) and DFI (bottom) featuring the optimized duct configuration (D = 2 mm; L = 10 mm; G = 1 mm; blunt inlet). Operating conditions: vessel pressure = 57.3 bar; vessel temperature = 900 K; rail pressure = 1200 bar.

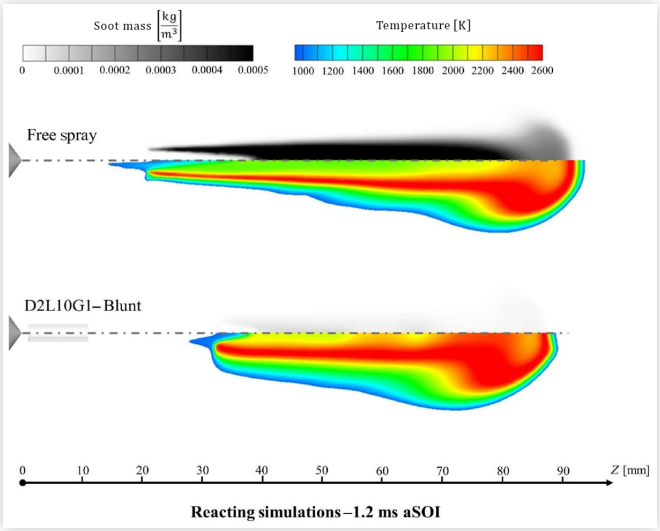

© Politecnico di Torino

outcomes of the herein simulation analysis in a constant-volume vessel can be summarized as follows:

- The reduction of both stand-off distance and duct length improves the soot mitigation performance due to the higher turbulent mixing effectiveness and the lower collision length until the upstream air entrainment becomes negligible and the LOL is quite close to the duct exit.
- Large duct diameters could change DFI operation leading to ignition within the duct volume; while small duct diameters tend to reduce the upstream air entrainment, decreasing DFI benefits. A trade-off is therefore necessary.
- A chamfer at the duct inlet can improve DFI performances, promoting higher upstream air entrainment and extending the LOL. On the other side, the tapered outlet does not lead to significant improvements.
- From a general point of view, each evaluated duct geometry results in lower soot emissions than free spray configuration, ranging between 43% and 94% of relative reduction, apart from the case of in-duct combustion. In this latter case, the DFI benefits are completely deleted making DFI combustion more sooting than free-spray one.

Results have shown that DFI combustion and soot formation are very sensitive to duct geometrical variations; thereby, duct geometry optimization in engine application is mandatory. Furthermore, a comprehensive study on the effect of operating conditions and calibration parameters on DFI performance is necessary for assessing the robustness of the optimal duct geometry and will be an object of future studies.

Acknowledgments

The Authors would like to acknowledge General Motors (GM) and PUNCH Torino for sponsoring the Research Activity.

Computational resources provided by hpc@polito, which is a project of Academic Computing within the Department of Control and Computer Engineering at the Politecnico di Torino (http://hpc.polito.it).

Contact Information

Prof. Federico Millo
Politecnico di Torino | Energy Department (DENERG)
Corso Duca degli Abruzzi, 24 | 10129 Torino (IT)
federico.millo@polito.it

Abbreviations

aSOI - after Start of Injection
CFD - Computational Fluid Dynamics
CI - Compression-Ignition
CVV - Constant-Volume Vessel
DFI - Ducted Fuel Injection
DoE - Design of Experiments
ECN - Engine Combustion Network
EGR - Exhaust Gas Recirculation
HCCI - Homogeneous-Charge Compression-Ignition
HRR - Heat Release Rate
IMEP - Indicated Mean Effective Pressure
LLFC - Leaner Lifted-Flame Combustion
LOL - Lift-Off Length
LTC - Low Temperature Combustion
MC - Mixing-Controlled
NOx - Nitrogen Oxides
PAHs - Polycyclic Aromatic Hydrocarbons
PDA - Phase-Doppler Anemometry
PM - Particulate Matter
RANS - Reynolds-Averaged Navier-Stokes
RCCI - Reactivity-Controlled Compression-Ignition
TKE - Turbulent Kinetic Energy
A - Area
D - Duct diameter
G - Stand-off distance

Downloaded from SAE International by Torino Politecnico, Tuesday, September 28, 2021

L - Duct length
P - Pressure
T - Temperature
V - Velocity
Z - Spray axis
$\dot{m}$ - Mass flow rate
ϕ - Equivalence ratio

References

1. Janssen, N.A., Gerlofs-Nijland, M.E., Lanki, T. et al., *Health Effects of Black Carbon* (Copenhagen: WHO, 2012).
2. Bond, T.C., Doherty, S.J., Fahey, D. et al., "Bounding the Role of Black Carbon in the Climate System: A Scientific Assessment," *J. Geophys. Res. Atmos.* 118, no. 11 (2013): 5380-5552, https://doi.org/10.1002/jgrd.50171.
3. Miller, J. and Jin, L., "Global Progress toward Soot-Free Diesel Vehicles in 2019," in *ICCT*, Xi'an, China, 2019.
4. Brizi, G., Postrioti, L., and van Vuuren, N., "Experimental Analysis of SCR Spray Evolution and Sizing in High-Temperature and Flash Boiling Conditions," *SAE Int. J. Fuels Lubr.* 12, no. 2 (2019): 87-107, https://doi.org/10.4271/04-12-02-0006.
5. Millo, F., Rafigh, M., Sapio, F. et al., "Modeling NOx Storage and Reduction for a Diesel Automotive Catalyst Based on Synthetic Gas Bench Experiments," *Ind. Eng. Chem. Res.* 57, no. 27 (2018): 12335-12351, https://doi.org/10.1021/acs.iecr.8b01813.
6. Patterson, M.A., Kong, S.C., Hampson, G.J., and Reitz, R.D., "Modeling the Effects of Fuel Injection Characteristics on Diesel Engine Soot and NOx Emissions," SAE Technical Paper 940523, 1994, https://doi.org/10.4271/940523.
7. Musculus, M.P.B., Miles, P.C., and Pickett, L.M., "Conceptual Models for Partially Premixed Low-Temperature Diesel Combustion," *Prog. Energy Combust. Sci.* 39 (2013): 246-283, https://doi.org/10.1016/j.pecs.2012.09.001.
8. Fuquan, Z., Assanis, D.N., Asmus, T.N., Dec, J. et al., *Homogeneous Charge Compression Ignition (HCCI) Engines: Key Research and Development Issues* (Warrendale, PA: Society Automotive Engineers, 2003).
9. Reitz, R.D. and Duraisamy, G., "Review of High Efficiency and Clean Reactivity Controlled Compression Ignition (RCCI) Combustion in Internal Combustion Engines," *Prog. Energy Combust. Sci.* 46 (2015): 12-71, https://doi.org/10.1016/j.pecs.2014.05.003.
10. Kamimoto, T. and Bae, M.H., "High Combustion Temperature for the Reduction of Particulate in Diesel Engines," SAE Technical Paper 880423, 1988, https://doi.org/10.4271/880423.
11. Pickett, L.M. and Siebers, D.L., "Non-Sooting, Low Flame Temperature Mixing-Controlled DI Diesel Combustion," SAE Technical Paper 2004-01-1399, 2004, https://doi.org/10.4271/2004-01-1399.
12. Polonowski, C., Mueller, C., Gehrke, C., Bazyn, T. et al., "An Experimental Investigation of Low-Soot and Soot-Free Combustion Strategies in a Heavy-Duty, Single-Cylinder, Direct-Injection, Optical Diesel Engine," *SAE Int. J. Fuels Lubr.* 5, no. 1 (2012): 51-77, https://doi.org/10.4271/2011-01-1812.
13. Mueller, C.J., Nilsen, C.W., Ruth, D.J. et al., "Ducted Fuel Injection: A New Approach for Lowering Soot Emissions from Direct-Injection Engines," *Appl. Energy* 204 (2017): 206-220, https://doi.org/10.1016/j.apenergy.2017.07.001.
14. Gehmlich, R.K., Mueller, C.J., Ruth, D.J. et al., "Using Ducted Fuel Injection to Attenuate or Prevent Soot Formation in Mixing-Controlled Combustion Strategies for Engine Applications," *Appl. Energy* 226 (2018): 1169-1186, https://doi.org/10.1016/j.apenergy.2018.05.078.
15. Nilsen, C.W., Biles, D.E., and Mueller, C.J., "Using Ducted Fuel Injection to Attenuate Soot Formation in a Mixing-Controlled Compression Ignition Engine," *SAE Int. J. Engines* 12, no. 3 (2019): 309-322, https://doi.org/10.4271/03-12-03-0021.
16. Nilsen, C.W., Biles, D.E., Yraguen, B.F., and Mueller, C.J., "Ducted Fuel Injection versus Conventional Diesel Combustion: An Operating-Parameter Sensitivity Study Conducted in an Optical Engine with a Four-Orifice Fuel Injector," *SAE Int. J. Engines* 13, no. 3 (2020): 345-362, https://doi.org/10.4271/03-13-03-0023.
17. Nilsen, C.W., Biles, D.E., Yraguen, B.F., and Mueller, C.J., "Ducted Fuel Injection vs. Conventional Diesel Combustion: Extending the Load Range in an Optical Engine with a Four-Orifice Fuel Injector," *SAE Int. J. Engines* 14, no. 1 (2021): 47-58, https://doi.org/10.4271/03-14-01-0004.
18. Li, F., Lee, C., Wu, H. et al., "An Optical Investigation on Spray Macroscopic Characteristics of Ducted Fuel Injection," *Exp. Therm. Fluid Sci.* 109 (2019): 109918, https://doi.org/10.1016/j.expthermflusci.2019.109918.
19. Li, F., Lee, C., Wang, Z. et al., "Optical Investigation on Impacts of Ambient Pressure on Macroscopic Spray Characteristics of Ducted Fuel Injection under Non-Vaporizing Conditions," *Fuel* 268, no. 5 (2020): 117192, https://doi.org/10.1016/j.fuel.2020.117192.
20. Li, F., Lee, C., Wang, Z. et al., "Schlieren Investigation on Impacts of Duct Size on Macroscopic Spray Characteristics of Ducted Fuel Injection," *Appl. Therm. Eng.* 176, no. 8 (2020): 115440, https://doi.org/10.1016/j.applthermaleng.2020.115440.
21. Svensson, K.I. and Martin, G.C., "Ducted Fuel Injection: Effects of Stand-Off Distance and Duct Length on Soot Reduction," *SAE Int. J. Adv. Curr. Pract. in Mobility* 1, no. 3 (2019): 1074-1083, https://doi.org/10.4271/2019-01-0545.
22. Fitzgerald, R.P., Svensson, K., Martin, G., Qi, Y. et al., "Early Investigation of Ducted Fuel Injection for Reducing Soot in Mixing-Controlled Diesel Flames," *SAE Int. J. Engines* 11, no. 6 (2018): 817-833, https://doi.org/10.4271/2018-01-0238.

Downloaded from SAE International by Torino Politecnico, Tuesday, September 28, 2021

23. Tanno, S., Kawakami, J., Kitano, K., and Hashizume, T., "Investigation of a Novel Leaner Fuel Spray Formation for Reducing Soot in Diffusive Diesel Combustion-Homogenizing Equivalence Ratio Distribution in the Lift-Off Region," SAE Technical Paper 2019-01-2273, 2019, https://doi.org/10.4271/2019-01-2273.
24. Nilsen, C.W., Yraguen, B.F., Mueller, C.J., Genzale, C. et al., "Ducted Fuel Injection vs. Free-Spray Injection: A Study of Mixing and Entrainment Effects Using Numerical Modeling," *SAE Int. J. Engines* 13, no. 5 (2020): 705-715, https://doi.org/10.4271/03-13-05-0044.
25. Millo, F., Piano, A., Peiretti Paradisi, B. et al., "Ducted Fuel Injection: Experimental and Numerical Investigation on Fuel Spray Characteristics, Air/Fuel Mixing and Soot Mitigation Potential," *Fuel* 289 (2021): 119835, https://doi.org/10.1016/j.fuel.2020.119835.
26. Millo, F., Segatori, C., Piano, A., Peiretti Paradisi, B. et al., "An Engine Parameters Sensitivity Analysis on Ducted Fuel Injection in Constant Volume Vessel Using Numerical Modeling," SAE Technical Paper 2021-24-0015, 2021, https://doi.org/10.4271/2021-24-0015.
27. Piano, A., Millo, F., Postrioti, L., Biscontini, G. et al., "Numerical and Experimental Assessment of a Solenoid Common-Rail Injector Operation with Advanced Injection Strategies," *SAE Int. J. Engines* 9, no. 1 (2016): 565-575, https://doi.org/10.4271/2016-01-0563.
28. Richards, K.J., Senecal, P.K., and Pomraning, E., "CONVERGE 2.4," Convergent Science, Madison, WI, 2018.
29. Yakhot, V. and Orszag, S.A., "Renormalization Group Analysis of Turbulence. I. Basic Theory," *J. Sci. Comput.* 1, no. 1 (1986): 3-51, https://doi.org/10.1007/BF01061452.
30. Reitz, R.D. and Diwakar, R., "Structure of High-Pressure Fuel Sprays," SAE Technical Paper 870598, 1987, https://doi.org/10.4271/870598.
31. Amsden, A.A., O'Rourke, P.J., and Butler, T.D., "KIVA-II: A Computer Program for Chemically Reactive Flows with Sprays," LA-11560-MS, Los Alamos Natl. Lab. Tech., Los Alamos, NM, 1989.
32. Reitz, R.D. and Bracco, F.V., "Mechanisms of Breakup of Round Liquid Jets," in *Encyclopedia of Fluid Mechanics* (Houston: Gulf Pub. Co., Book Division, 1986), https://inis.iaea.org/search/search.aspx?orig_q=RN:19041515.
33. Liu, A.B., Mather, D., and Reitz, R.D., "Modeling the Effects of Drop Drag and Breakup on Fuel Sprays," SAE Technical Paper 930072, 1993, https://doi.org/10.4271/930072.
34. Naber, J.D. and Reitz, R.D., "Modeling Engine Spray/Wall Impingement," SAE Technical Paper 880107, 1988, https://doi.org/10.4271/880107.
35. Amsden, A.A. and Findley, M., *KIVA-3V: A Block-Structured KIVA Program for Engines with Vertical or Canted Valves* (Washington, DC: US Department of Energy, 1997).
36. Zeuch, T., Moréac, G., Ahmed, S.S., and Mauss, F., "A Comprehensive Skeletal Mechanism for the Oxidation of n-Heptane Generated by Chemistry-Guided Reduction," *Combust. Flame* 155, no. 4 (2008): 651-674, https://doi.org/10.1016/j.combustflame.2008.05.007.
37. Mauss, F., *Entwicklung eines kinetischen Modells der Rußbildung mit schneller Polymerisation* (Göttingen: Cuvillier, 1997)
38. Kazakov, A. and Frenklach, M., "Dynamic Modeling of Soot Particle Coagulation and Aggregation: Implementation with the Method of Moments and Application to High-Pressure Laminar Premixed Flames," *Combust. Flame* 114 (1998): 484, https://doi.org/10.1016/S0010-2180(97)00322-2.
39. Siebers, D. and Higgins, B., "Flame Lift-Off on Direct-Injection Diesel Sprays under Quiescent Conditions," SAE Technical Paper 2001-01-0530, 2001, https://doi.org/10.4271/2001-01-0530.
40. Higgins, B. and Siebers, D., "Measurement of the Flame Lift-Off Location on DI Diesel Sprays Using OH Chemiluminescence," SAE Technical Paper 2001-01-0918, 2001, https://doi.org/10.4271/2001-01-0918.
41. Rhim, D.R. and Farrell, P.V., "Characteristics of Air Flow Surrounding Non-Evaporating Transient Diesel Sprays," SAE Technical Paper 2000-01-2789, 2000, https://doi.org/10.4271/2000-01-2789.

© 2022 Politecnico di Torino; Published by SAE International. This Open Access article is published under the terms of the Creative Commons Attribution License (http://creativecommons.org/licenses/by/4.0/), which permits distribution, and reproduction in any medium, provided that the original author(s) and the source are credited.

Positions and opinions advanced in this work are those of the author(s) and not necessarily those of SAE International. Responsibility for the content of the work lies solely with the author(s).